Unravelling the morphological dependency of the LiNi0.6Mn0.2Co0.2O2 layered oxide reactivity in Li-ion batteries

Adrien Soloy, Delphine Flahaut, Jean-Bernard Ledeuil, Joachim Allouche, Dominique Foix, Germain Vallverdu, Emmanuelle Suard, Erwan Dumont, Lucille Gal, François Weill, et al.

Unravelling the morphological dependency of the $LiNi_{0.6}Mn_{0.2}Co_{0.2}O_2$ layered oxide reactivity in Li-ion batteries

Adrien Soloy[1], Delphine Flahaut[2,5], Jean-Bernard Ledeuil[2,5], Joachim Allouche[2,5], Dominique Foix[2,5], Germain Salvato Vallverdu[2,5], Emmanuelle Suard[3], Erwan Dumont[4], Lucille Gal[4], François Weill[1,5,6,] and Laurence Croguennec[1,5,6,*]*

[1] Univ. Bordeaux, CNRS, Bordeaux INP, ICMCB UMR 5026, F-33600 Pessac, France

[2] Université de Pau et des Pays de l'Adour, E2S UPPA, CNRS, IPREM UMR 5254, 64000 Pau, France

[3] Institut Laue-Langevin, 71 avenue des Martyrs, 38042 Grenoble, France

[4] SAFT, Direction de la Recherche, 33074 Bordeaux, France

[5] RS2E, Réseau Français sur le Stockage Electrochimique de l'Energie, FR CNRS 3459, F-80039 Amiens Cedex 1, France

[6] ALISTORE-ERI European Research Institute, FR CNRS 3104, F-80039 Amiens Cedex 1, France

KEYWORDS: Li-ion battery, Layered oxide, NMC, morphology, reactivity, performances

ABSTRACT

$LiNi_{0.6}Mn_{0.2}Co_{0.2}O_2$ is one of the most promising positive electrode material for Li-ion batteries. Platelet-shaped particles of 17 nm and 86 nm thickness were obtained, with the required composition and a structure close to the ideal 2D layered structure (less than 5.2% Ni^{2+} ions in Li^+ sites). The electrochemical performances and surface reactivity of the materials were characterized in Li-ion batteries and compared to that of 280 nm particles with a more conventional morphology. Post-cycling analyses revealed a particular reactivity at high potential for the platelets compared to the conventional particles. X-Ray photoelectron spectroscopy and *ex situ* XRD analyses were performed to characterize the composition of the positive electrode/electrolyte interface and the structural changes undergone by the three materials upon cycling respectively. This study showed that, as well as the particles' composition, their morphology plays a significant role regarding the reactivity and the structural changes occurring during cycling at high potential.

INTRODUCTION

The rapid development of the electric and hybrid vehicles industry caused an increasing demand for Li-ion batteries (LiBs) with high energy densities and low cost in the last decade. Indeed the global Li-ion cell manufacturing capacity was expected to increase between 4 and 6 times by 2021-2022 compared with 2017 levels.[1] The demand for LiBs is still expected to increase exponentially until 2030 thanks to the democratization of electric vehicles. By 2040, 50 times more electric vehicles are expected to be on the road compared to 2018.[1] One of the main challenges remains to find materials that can handle fast charge as the goal of the electric vehicle industry is to manage to decrease the charge duration of the vehicles to enable their use during long journeys. Layered oxides $LiMO_2$ (M= Ni, Mn, Co) are part of the best candidates as positive electrode materials for LiBs.[2] Among all the possible compositions, the $LiNi_{0.6}Mn_{0.2}Co_{0.2}O_2$ layered oxide (NMC622) was shown to be one of the best compromises to combine the beneficial effects of the Ni, Mn and Co for good energy density, structural and thermal stability and good cyclability respectively.[2] Many efforts have been made in the past twenty years to control the synthesis and properties of this material.[3–13] In order to optimize their electrochemical properties, different studies have been focused on preparing them with different morphologies (i.e. particle size or shape), especially as oriented or platelet-shaped particles in order to obtain materials that can handle fast charge.[6,11,12,14–22] Indeed, the platelet morphology tends to stabilize the {010} facets, that are the Li^+ ions diffusion pathways into the structure, so it enhances the alkali diffusion during cycling and increases the performances of the material.[11,12] A further enhancement of the electrochemical performances has been observed when these platelets are radially oriented inside secondary particles as this particular morphology is the best one to maximize the access to the diffusion paths.[16] Such morphologies are mostly obtained by coprecipitation[6,16–18,21,22] or hydrothermal

synthesis[11,12,15] followed by a solid-state reaction at high temperature. Regardless of the synthesis method chosen, the growth of platelet particles requires the use of a surfactant that will adsorb preferentially on specific facets of the particles and impede the growth of the particles in one particular direction.[18] The most usual surfactants are cetyltrimethylammonium bromide (CTAB)[12], sodium dodecyl sulfate (SDS)[11,15], polyvinylpyrrolidone (PVP)[20–22] and ammonium hydroxide (NH_4OH).[6,16–18] NH_4OH is a reactant commonly used during coprecipitation as a chelating agent but it was shown by Hua et al. that it could also play the role of a surfactant when it is used in large amount.[18]

In this study, NMC622 samples with platelet-shaped particles were synthesized using the NH_4OH-assisted coprecipitation method. Their electrochemical performances and reactivity were studied and compared with particles with a more conventional morphology. Indeed, despite numerous studies were already performed on NMC622 with platelet morphology. The surface reactivity versus the electrolyte of NMC622 materials, depending on their morphology, still requires to be studied for an optimization of their performance in Li-ion batteries. The aim of this work is thus to get better insight into the relationship between the particles' morphology of NMC622 materials with controlled composition and structure, their electrochemical performances and their reactivity in organic liquid electrolyte.

EXPERIMENTAL SECTION

The synthesis of $Ni_{0.6}Mn_{0.2}Co_{0.2}(OH)_2$ hydroxide was made by coprecipitation using the same synthesis protocol to that described in one of our previous works,[23] using a 0.36 mol/L NH_4OH (Sigma-Aldrich, 28-30%) aqueous solution to obtain the transition metal hydroxide precursor of the NMC622 with conventional particles, and using a highly concentrated 5

mol/L NH_4OH aqueous solution to obtain the transition metal hydroxide precursor of the NMC622 with platelet particles of different thicknesses. **Figure S1** given in supplementary information shows the XRD patterns and SEM pictures of the mixed transition metal hydroxide precursors obtained in the two conditions. These mixed transition metal (TM) hydroxides are intimately mixed with lithium carbonate Li_2CO_3 (Sigma-Aldrich, ≥99%) to prepare three different lithiated transition metal oxides NMC622. A thermal treatment of the $Ni_{0.6}Mn_{0.2}Co_{0.2}(OH)_2/Li_2CO_3$ mixture is performed at high temperature, under air, and with a Li/TM ratio of 1.05 (an additional 5 wt.% Li_2CO_3 excess is added to ensure this ratio despite Li loss during the synthesis). This slight overlithiation (i.e. Li/TM ≥ 1.05) is required to obtain a layered structure with the smallest amount of Ni^{2+} ions in the Li sites. Two platelet-type layered oxide samples obtained at 780°C (sample 17-PL) and 810°C (sample 86-PL) are compared to a conventional material obtained at 870°C (sample 870-5-air).[23] **Figure S2** shows how the XRD patterns and morphologies of the samples evolve with the temperature of the thermal treatment, when the mixed TM hydroxide is obtained from the highly concentrated 5 mol/L NH_4OH solution. This preliminary study revealed that the higher the temperature, the less 2D is the layered structure (as shown for instance by the decreasing (003)/(104) line intensity ratio[23]) and the thicker are the platelets. These results explain the temperatures chosen for the thermal treatment to obtain the platelet-like layered oxide samples, i.e. 780°C and 810°C.

The cationic composition of the lithiated layered oxides was determined by Inductively Coupled Plasma - Optical Emission Spectrometry (ICP-OES) (Varian ICP/OES 720 ES) and the carbon content of the powders was determined using a CHNS elemental Thermo Fischer Scientific analyser equipped with an automatic sampler. The detail protocol has already been described in a previous work.[23]

To identify the phases contained in the samples and to determine the crystallographic structure of the layered oxides, powder X-Ray diffraction (XRD) patterns were recorded using a PANalytical X'Pert PRO MPD diffractometer equipped with a Cu radiation X-ray tube, and the powder neutron diffraction (NPD) patterns using the high-resolution powder diffractometer D2B at Institut Laue Langevin (ILL, Grenoble, France). The XRD patterns were collected in the angular range of 10-80°(2θ) with 0.008° intervals, for a total acquisition time of around 35 hrs, whereas the NPD patterns were collected at room temperature with a wavelength $\lambda = 1.5947(1)$ Å, in the angular range of 0-160° (2θ) with 0.05° intervals, for a total acquisition time of around 5 hrs. For NPD the powders were contained in a vanadium tube with a diameter of 8 mm. The collected XRD and NPD patterns were refined by the Rietveld method using FullProf software.[24] The peaks' profiles were described by a Pseudo-Voigt function and the full width at half maximum by a Caglioti function. For the NPD patterns, due to the geometry of the diffractometer (transmission mode), a correction factor μR of 0.79 was applied to take into account the absorption of the signal.[25] XRD patterns were also collected to study structural changes in electrode materials recovered from coin cells after cycling, using a Philips PW1820 diffractometer equipped with a Cu radiation X-ray tube. The electrodes were fixed with a Kapton tape in a hygroscopic sample-holder made of aluminium alloy and Kapton windows. The XRD patterns were collected in the angular range of 5-80°(2θ) with 0.02° intervals, for a total acquisition time of around 10 hrs.

The particles morphology and size were observed by scanning electron microscopy (Hitachi S4500 FEG), after being metallized by gold deposition. Transmission electron microscopy (JEOL JEM-2100) and Selected Area Electron Diffraction (SAED) were performed to get information on the nature of the faces. BET surface areas were determined using a

Micromeritics 3FLEX analyser, after degassing the powders under vacuum at 90°C for 1 hr and then at 150°C for 10 hrs.

X-ray Photoelectron Spectroscopy (XPS) has been used to determine the surface composition of the pristine powders using a Kratos Axis Ultra DLD spectrometer, of the pristine electrodes using an ESCALAB 250 Xi spectrometer, and of cycled electrodes using a Thermo Scientific K-Alpha spectrometer. A monochromatized Al-Kα X-Ray source (hν = 1486.6 eV) has been used with a neutraliser gun to minimize surface charging. For the pristine powders, the spectral calibration was carried out using the C-C/C-H component (285.0 eV) originated from the usual surface carbon contamination in C1s core peaks. For the cycled electrodes, it was carried out using the CF_2 component (291.0 eV) originated from the PVDF polymeric binder in C1s core peaks. The peak fitting process was carried out using a non-linear Shirley-type background. The peak positions and areas were optimized by weighted least-squares calculation method using 70% Gaussian and 30% Lorentzian line shapes. The quantification of surface composition was performed using basis of Scofield's relative sensitivity factors corrected by specific values depending on the apparatus.[26] The quantification and spectra fitting were carried out using CASA XPS software.

Auger Electron Spectroscopy (AES) and Scanning Auger Mapping (SAM) were carried out with a JEOL JAMP 9500F Auger Microprobe spectrometer (JEOL Ltd, Tokyo, Japan) working under UHV conditions (pressure < $2 .10^{-7}$ Pa). The UHV equipment was a Schottky field emission Auger electron spectrometer (FE-AES) dedicated to very high spatial resolution analysis and high brightness. The hemi-spherical electron analyzer coupled with a multichannel detector (7 channeltrons) offered ideal settings for energy resolved Auger analysis. SEM images, SAM images and Auger spectra were recorded using an acceleration

voltage of 10 keV, a probe current of 3 nA and a working distance at 23 mm (sample tilt angle = 45°). Spectra (kinetic energy from 0 to 1000 eV) were carried out at a constant retarding ratio (CRR) mode with dE/E = 0.5% (high sensibility). The reference spectra of MnO, LiF and CoO were taken from the JEOL standard materials reference database. The SAM images were performed in constant retarding ratio (CAE) operating conditions to enable defining the useful energy width needed to obtain a significant peak background-intensity difference with respect to the Auger transition and the background shape. An "auto probe tracking" correction was also used to control and compensate the drift due to the balance of sample surface charge effects and instrument-dependent fluctuations.

Evaluation of the electrochemical performances was done in CR2032-type coin cells versus a lithium metal foil as negative electrode. The positive electrodes were prepared by coating a slurry on an aluminium foil as current collector. The slurry was prepared by mixing the active material with the carbon black and the polyvinylidene fluoride (PVDF, Sigma, average Mw ≈ 534000 g/mol by Gel Permeation Chromatography (GPC)) binder (92:4:4 wt.%) in N-methyl-2-pyrrolidone (NMP) (Sigma Aldrich, 99%). The electrolyte was 1 mol/L $LiPF_6$ dissolved in a mixture of dimethyl carbonate (DMC) and fluoro ethylene carbonate (FEC) in a 70/30 volume ratio. The coin cells were assembled in an argon-filled glovebox and were cycled using a VMP (Biologic) in galvanostatic mode. Galvanostatic Intermittent Titration Technique (GITT) experiments were performed at a constant current pulse of C/100 for 30 min and then rest for 15 hrs to stabilize the cell voltage between 2.5 and 4.6 V. Coin cells were dismantled after cycling in an Ar-filled glovebox to recover the electrodes, which were washed 3 times with an excess of DMC and dried under vacuum.

RESULTS AND DISCUSSION

Structural and physico-chemical characterizations

Figure 1 depicts the XRD patterns collected for three different NMC622 layered oxides, two of them with platelet-type morphologies (17-PL and 86-PL) as it will be shown hereafter and the latter with a conventional morphology (870-5-air). The three samples appear from XRD as pure layered oxides; all the diffraction lines can be indexed in an α-$NaFeO_2$-type layered structure described in the R-3m space group. The peaks' widths are significantly larger for the platelet-type materials 17-PL and 86-PL, reflecting smaller crystallites compared to the conventional material 870-5-air, as shown by the larger Full Width at Half Maximum (FWHM) values reported in **Table 1** for the (003), (104) and (110) peaks. The $I_{(003)}/I_{(104)}$ intensity ratios for the three materials are also reported in this table. The lower $I_{(003)}/I_{(104)}$ ratio obtained for the 86-PL sample reflects a less 2D layered structure compared to the two other materials.

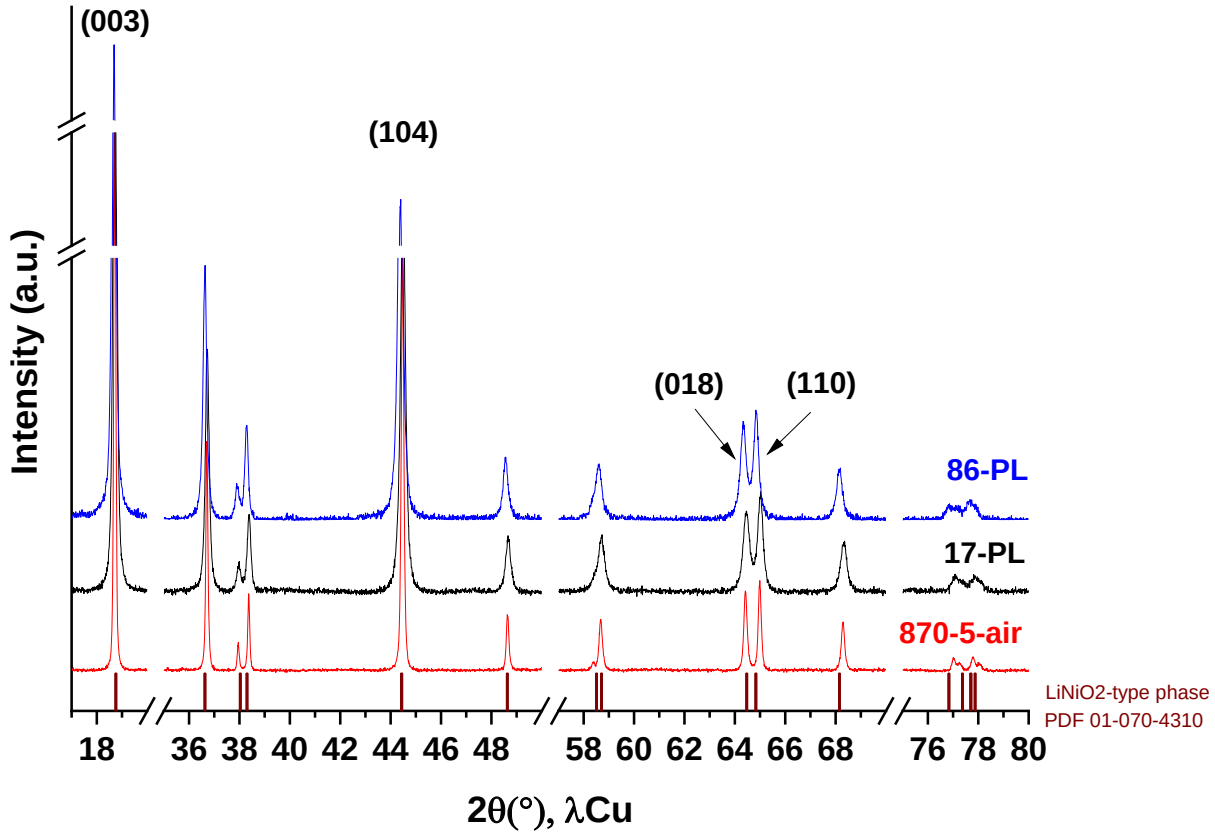

Figure 1. X-ray diffraction patterns obtained for the platelet-type layered oxide samples synthesized at 810°C (86-PL, blue) and at 780°C (17-PL, black), compared to that of the sample of conventional morphology and obtained in regular conditions (870-5-air, red).

The experimental stoichiometry in transition metals, as determined by chemical analyses performed by ICP-OES, is close to the expected one for the three samples (**Table S1**). The slight overlithiation required to obtain the layered structure is obtained for the three materials with Li/TM ratios larger than 1. As in one of our previous works, we notice that the Li/TM ratio varies from 1.00 to 1.10 between the three samples whereas the same Li/TM ratio was used for the synthesis and the loss of Li does not seem to be linear with the increasing temperature of the thermal treatment.[23] Note that traces of carbon (≈1 wt.%) were found by CHNS analyses, probably associated to the presence of Li_2CO_3 coming either from the Li precursor used in excess during the synthesis or from the reaction of the material with air after

the synthesis.[27–29] This amount of carbon does not evolve continuously with the thermal treatment temperature nor the Li/TM ratio.

In the layered oxide type structures, it is known that some transition metal ions can be present in the lithium site, reducing the 2D character of the material.[10,30–34] In such case, the amount and the nature of the transition metal can be determined by neutron diffraction. In Ni-rich layered oxides such as NMC622, this transition metal was shown to be Ni^{2+} ions.[35–38] A combined structural refinement based on X-ray and neutron diffraction data has been undertaken to determine the cation distribution between the Lithium site (i.e. within the interslab spaces) and the transition metal site (i.e. within the slabs). **Figure S3** shows, as an example, the results obtained for the 17-PL sample, whereas **Table S2** gathers the structural parameters. A small amount of Ni^{2+} ions (2.7%) is found to be present in the Li-3b site. **Table 1** compares the lattice parameters and the cationic distributions determined by the Rietveld refinement for the three NMC622 layered oxides studied in this work. The proposed cationic distributions take into account the charge balance, the presence of Ni^{2+} ions in the interslab space as evidenced by the neutron diffraction and preferential stabilization of trivalent and tetravalent states for the Cobalt and Manganese ions respectively in these structures and synthesis conditions.[34] It reveals, for the 86-PL sample for example, that 5.2% Ni^{2+} ions occupy the Li sites, inducing a theoretical capacity of 273 mAh/g ($Q_{th} = \frac{n_{e-}F}{3{,}6*M_{host}}$) corresponding to 0.948 Li^{+} ions exchanged per formula unit.

Figure 2 compares scanning electron micrographs typical of the three samples and the corresponding size distributions determined manually by the measure of the size of 100 particles.

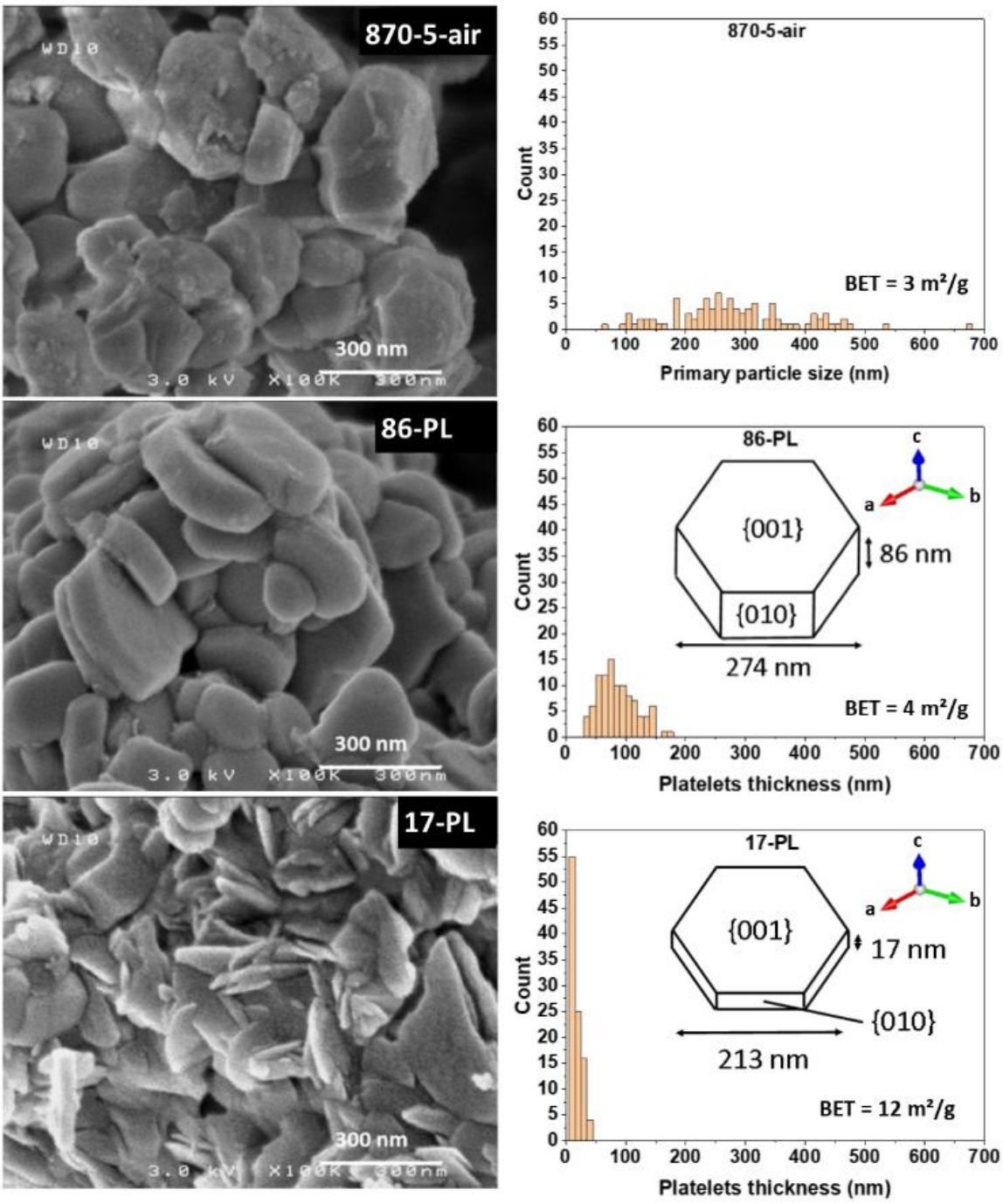

Figure 2. On the left, morphologies of the 870-5-air (particles of conventional morphology and being 280 nm in diameter), 17-PL (17 nm thick and 213 nm long platelets) and 86-PL (86 nm thick and 274 nm long platelets) samples illustrated by SEM images; On the right, corresponding size distributions determined considering 100 particles. Values of specific surface areas and schemes with the dimensions of the platelets are also given for comparison.

Table 1. Comparison of the lattice parameters, c/a ratios, compositions and cation distributions calculated from the Rietveld refinements of the X-ray diffraction patterns

	a (b) (Å)	c (Å)	c/a	FWHM (003)	FWHM (104)	FWHM (110)	I(003)/ I(104)	Composition and cation distribution
86-PL	2.87248(9)	14.225(1)	4.9522(5)	0.16	0.21	0.25	1.52	$(Li_{0.948(3)}Ni^{2+}_{0.052(3)})(Ni^{2+}_{0.262(4)}Ni^{3+}_{0.317(5)}Mn^{4+}_{0.210(1)}Co^{3+}_{0.210(1)})O_2$
17-PL	2.86658(9)	14.208(1)	4.9564(5)	0.16	0.23	0.25	1.82	$(Li_{0.973(3)}Ni^{2+}_{0.027(3)})(Ni^{2+}_{0.232(4)}Ni^{3+}_{0.357(5)}Mn^{4+}_{0.205(1)}Co^{3+}_{0.205(1)})O_2$
870-5-air	2.86778(6)	14.2160(5)	4.9571(3)	0.08	0.12	0.14	1.81	$(Li_{0.966(3)}Ni^{2+}_{0.034(3)})(Ni^{2+}_{0.241(4)}Ni^{3+}_{0.346(5)}Mn^{4+}_{0.207(1)}Co^{3+}_{0.207(1)})O_2$

The 870-5-air sample consists of primary particles of 280 nm of diameter in average while the two other samples consist of platelet-shaped particles of 17 nm and 86 nm of thickness in average at 780°C and 810°C respectively (**Figure 2**) and 213 nm and 274 nm of length in average (**Figure S4**). When lithiations are performed at higher temperatures, the thickness of the platelets is increased while their length evolve less significantly, in accordance with Fu et al. works.[22] As reported in **Figure 2**, an increase of the specific surface area is observed when the particles' morphology is modified from conventional shapes to thin platelets, from 3 to 12 m^2/g.

To confirm the nature of the crystallographic facets of these platelets selected area electron diffraction (SAED) was performed, the example of the 17 nm thick platelets (17-PL) is given in **Figure 3**. **Figure 3a** shows two platelets placed on their lateral faces, showing a larger thickness than the average one, of around 70 and 50 nm. The grey circle highlights the area selected to perform electron diffraction. The direction identified in **Figure 3b** corresponds to the reciprocal c* direction, which demonstrates the thickness of the platelets is along the c direction and that the frontal plane of the particles is the (001) plane. This shows that the surfactant preferentially adsorbs on the (001) planes, stops the growth of the particle along the c axis and favours it in the (a,b) plane orthogonal to the c direction, as illustrated in **Figure 2** and in accordance with the mechanism unravelled by Hua et al.[18]

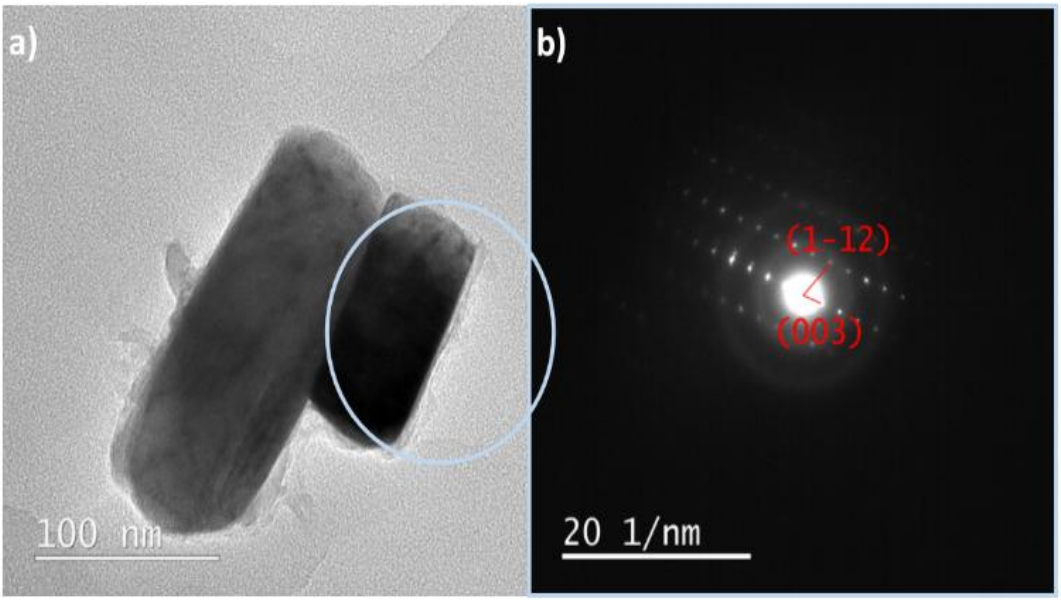

Figure 3. TEM image (a) and Selected Area Electron Diffraction (SAED) (b) performed on the lateral facets of two of the 17 nm thick platelets (17-PL), showing larger thicknesses than the average one.

By varying the synthesis conditions, three NMC622 layered oxides with a structure close to the ideal 2D layered structure (with less than 5.2% Ni^{2+} ions in the interslab spaces) and with different morphologies were obtained. One material shows conventional particles of 280 nm in average diameter while the two other materials are made of platelet-shaped particles of 7 nm and 86 nm thick in average. The platelets were grown in the (a,b) plane orthogonal to the c axis, as desired.

Surface analyses

To get a better knowledge of the chemical composition of the surface of the materials, analyses by XPS were performed. **Figure 4** compares the C1s, Li1s and O1s spectra obtained for the three samples.

From the CO_3^{2-} component observed at 290.1 eV in the C1s spectra and that of lithium in a carbonate at 55.5 eV in the Li1s spectra, the presence of Li_2CO_3 at the surface of the particles has been identified and quantified. The results are reported on **Figure 4** for the three materials and the complete quantitative analysis is given in **Table S3** for the 870-5-air sample. We can note that the contribution of oxygen from the NMC622 material (at 529.7 eV) in the O1s spectra is larger for the platelet-type materials (~ 10.8 ± 0.4 at.%) than for the 870-5-air one (3.2 at.%) with conventional particles. From these results it appears that the platelet-shape particles have less lithium carbonate at their surface than the conventional particles. Ni3p, Co3p, Li1s and Mn3p core peaks have been identified for which the peak maxima are located at 67.8 eV, 61.3 eV, 55.4 eV and 50.0 eV. On the basis of literature, the Ni3p core peak at 67.8 eV corresponds to nickel in a mixed valence Ni^{2+}/Ni^{3+}, the Co3p core peak at 61.3 eV corresponds to Co^{3+} and the Mn3p core peak at 50.0 eV corresponds to Mn^{4+} in an oxygen environment.[39,40] Even if the spectra corresponding to Ni, Co and Mn contributions are not very intense due to the presence of the carbonate layer, the quantification of these elements leads to a surface composition similar to that of the bulk, with transition metal stoichiometry varying between 6:2:2 and 6:1:3 (**Table S4**). Note that we used for this quantitative analysis the 3p core peaks since they are in the same binding energy range (45-80 eV) as opposed to the 2p core peaks.

As XRD measurements did not show the presence of any impurity and as only a very small amount of carbon (< 1 wt.%) was detected by gas phase chromatography, we believe Li_2CO_3 detected by XPS is only located as a thin layer at the extreme surface of the particles. No obvious relationship exists between the quantity of Li_2CO_3 determined by XPS and, on one side, the amount of Ni^{2+} ions present in the interslab space as determined for these three NMC622 materials by Rietveld refinement and, on the other side, their specific surface area. Nevertheless, the difference appears clearly between the conventional and the platelet-shaped particles showing {001} crystallographic oriented facets (**Figure 4**). As shown by Quesne-Turin et al., {001} facets of Li_2MnO_3 layered oxide preferentially consists, for the last layer, of transition metal slabs as terminal slabs rather than of Li ions interslabs.[41]

Similarly, we can assume that the {001} facets of our materials mainly consist of transition metal slabs. In the case of platelets with extended {001} facets, Li^+ ions would thus be less exposed to ambient air than for conventional particles so the formation of Li_2CO_3 is reduced, in good agreement with a lower amount of Li_2CO_3 at the surface of the platelets. It was shown by theoretical calculations on NMC compounds of different compositions that CO_2 would adsorb easily on (012) facets, that are the facets making an angle of 19° with the (010) facets, leading to the enhanced formation of carbonates.[42] Despite large carbonate contributions, intense signals coming from oxygen atoms in the NMC network (**Figure 4**) and transition metals (**Table S4**) are detected for the platelets. This induces that Li_2CO_3 may be organised in clusters, as nanoparticles at the surface of the platelets, probably mostly located on the more reactive lateral facets, without a uniform covering of the surface of the primary particles.

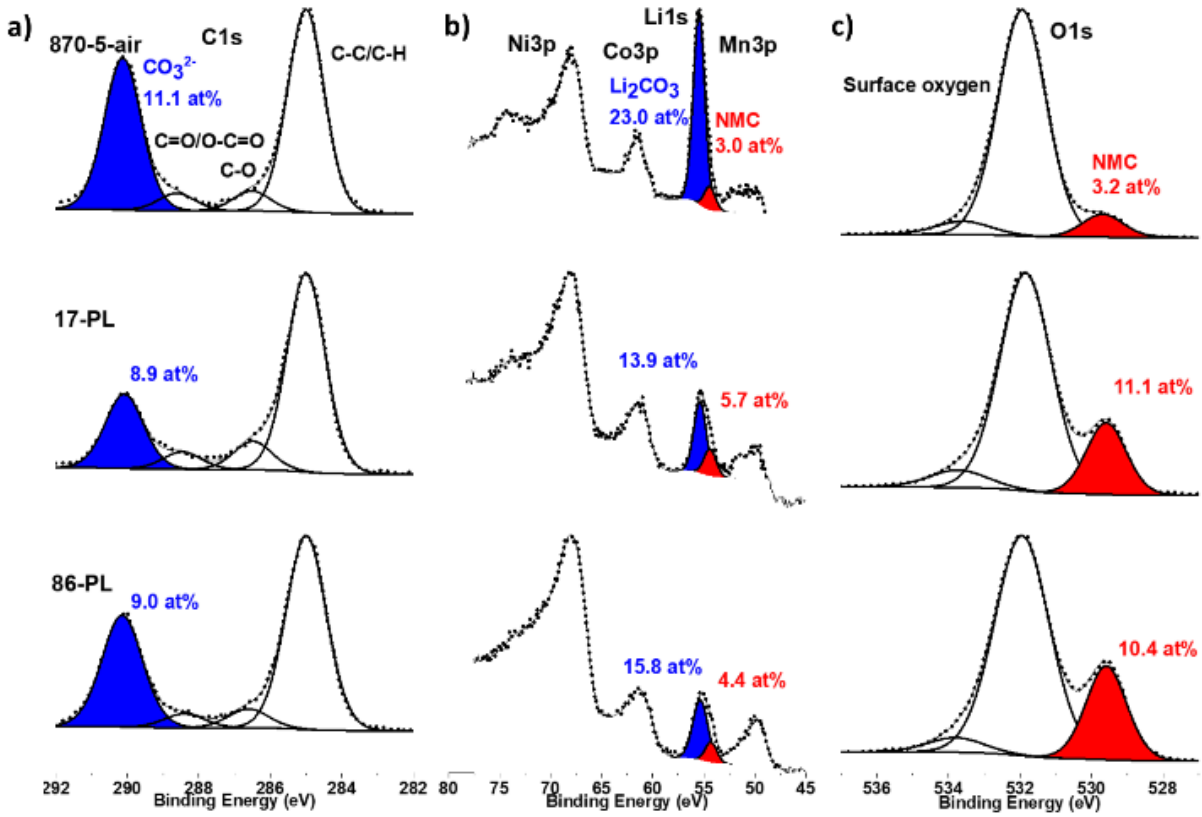

Figure 4. C1s (a), Li1s (b) and O1s (c) XPS spectra collected for the 870-5-air (conventional particles), 17-PL (17 nm thick platelets) and 86-PL samples (86 nm thick platelets). The C_{CO_3} and $Li_{Li_2CO_3}$ peaks are highlighted in blue and the O_{NMC} and Li_{NMC} peaks are highlighted in red. The dots and the lines represent the experimental and the fitted data respectively.

Electrochemical analyses

These samples were electrochemically tested in galvanostatic mode in CR2032 type coin cells versus Li. **Figure 5** shows the charge-discharge curves obtained for the three materials during the 1st cycle performed at the cycling rate of C/10 (1 charge or 1 discharge in 10 hrs) in the 2.5-4.3V potential range and **Figure S5** shows the corresponding dQ/dV=f(V) and V=f(x_{Li}) curves. The inset in **Figure 5** shows the evolution of the discharge capacities for the three materials when cycled at different rates (C/10, C/5, C, 2C and C/10 again, for 5 cycles at each

rate) as a function of the cycle number. The 1st discharge capacities and irreversible capacities (IRCs) are gathered in **Table 2**. As shown in **Figure S5a**, the polarization at 1st cycle is very similar for the 3 materials. During the 1st cycle, the material made of 17 nm thick platelets (17-PL) delivers a slightly larger 1st discharge capacity at C/10 of 156 mAh/g with the lowest IRC of 9% compared to the two other materials. Furthermore, whatever the cycling rate, ranging between C/10 and 2C, it shows the best performance, even if the difference with those delivered by the material made of conventional shape particles (870-5-air) is reduced with increasing cycling rate. The benefit of the platelet morphology is thus not as important as what could have been expected considering previous results published by Jiang et al. and Ju et al.[11,12]. This difference may probably be explained by the organization of the agglomerates: in references [11,12] the platelets are radially organised within spherical agglomerates so that the {010} faces are exposed to the electrolyte promoting fast Li^+ diffusion through the interslab spaces,[16] whereas in our case the platelet type particles are randomly distributed in the agglomerates decreasing the benefit of this particular morphology of the primary particles versus fast diffusion within the layered structure.

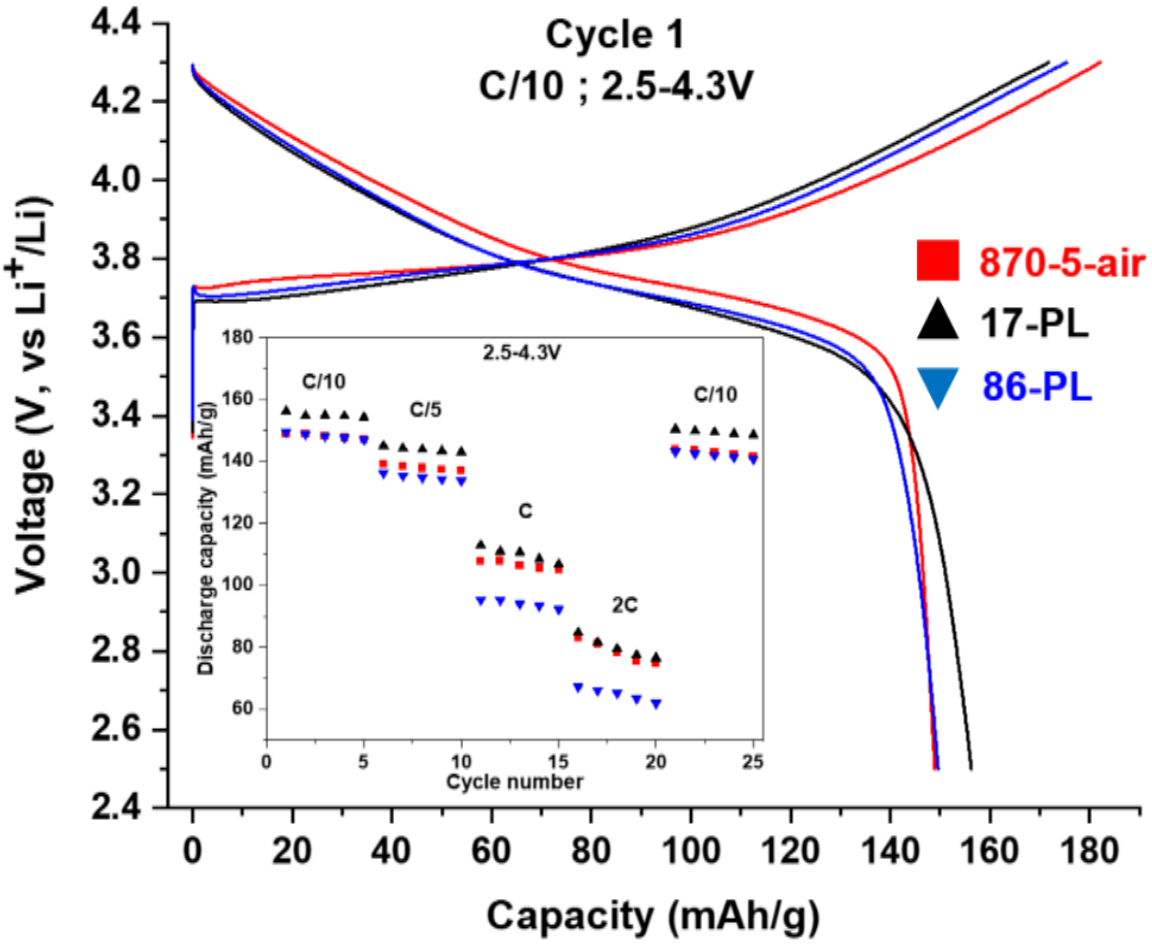

Figure 5. Charge-discharge curves obtained during the 1st cycle for the conventional particles (870-5-air, red line), the 17 nm thick platelets (17-PL, black line) and the 86 nm thick platelets (86-PL, blue line) when cycled at C/10 in the 2.5-4.3 V potential range. Evolution of the discharge capacities delivered by the three materials when cycled at C/10, C/5, C, 2C and C/10 for 5 cycles at each rate in the 2.5-4.3 V potential range (inset) (870-5-air, red squares), (17-PL, black triangles) and (86-PL, blue triangles).

Table 2. 1st discharge capacities and irreversible capacities (IRC, %) obtained for the three NMC622 materials when cycled at C/10 in the 2.5-4.3 V potential range and at C/5 in the 2.5-4.6 V potential range.

Sample	C/10 ; 2.5-4.3V		C/5 ; 2.5-4.6V	
	1st discharge capacity (mAh/g)	IRC (%)	1st discharge capacity (mAh/g)	IRC (%)
870-5-air (280 nm)	149	18	161	21
17-PL (17 nm thick platelets)	156	9	171	28
86-PL (86 nm thick platelets)	150	15	171	18

Other cycling tests were performed at a C-rate of C/5 (1 charge/discharge in 5 hrs) in a larger potential window of 2.5-4.6 V: the higher cut-off voltage potential was accompanied with an increase of the cycling rate in order to mitigate irreversible degradation of the electrolyte above 4.3 V vs. Li^+/Li. In these cycling conditions, the material made of 17 nm thick platelet type particles delivers the largest 1st charge and 1st discharge capacities among the three materials (**Figure 6** and **Table 2**). But it reveals also the lowest capacity retention compared to the materials made of conventional particles (870-5-air) and of thicker platelet type particles (86-PL), as shown in inset in **Figure 6**. In addition, as clearly observed in **Figure 6** and on the derivative curve dQ/dV given in **Figure S6a** in supplementary information, an irreversible oxidation is observed at the end of the first charge between 4.4 and 4.6 V vs. Li^+/Li for the material 17-PL with the thinner platelet type particles, this irreversible reaction inducing a large irreversible 1st discharge capacity (IRC) of 28% (**Table 2**). As seen by the evolution of this dQ/dV derivative curve upon cycling (**Figure S7**), this phenomenon is actually partly reversible with a small contribution in discharge at 4.53 V at 1st cycle and 4.47 V at 2nd cycle, and it disappears in the following cycles. Furthermore, an increasing overpotential is observed upon charge with a continuous shift towards higher potentials of the oxidation peak at 3.67 V for the 2nd cycle and at 3.72 V for the 40th cycle. Similarly, in discharge, the reduction peak observed at 4.25 V for the 2nd cycle shifts to 4.15 V for the 40th cycle. This irreversible oxidation could be associated to a drastic degradation of the

electrolyte during the 1st charge promoted by the high specific surface area of the 17-PL material (12 m^2/g versus less than 4 m^2/g for the two others), whereas the gradual formation of a resistive layer at the electrode/electrolyte interface would increasingly impede diffusivity of Li^+ ions within the structure and suppress this phenomenon in the following cycles. The reversible part of the phenomena could be linked to the H2→H3 phase transition occurring at this potential for NMC622.[43]

To better understand the behaviour observed for the 17 nm thick platelets (i.e. better performance in the 2.5-4.3 V potential window, whereas irreversible reaction at high voltage before fast performance degradation in the 2.5-4.6 V potential range), a comparative characterization of the three materials was performed upon cycling: by XRD to check for structural evolutions and by XPS to identify surface reactivity. In order to be as close as possible to the equilibrium and to promote all the irreversible reactions, coin cells were cycled in GITT conditions (slow C-rate of C/100 with intermediate relaxation periods) and were stopped at different states of charge and discharge during the 1st cycle: at 3.8 V, 4.3 V, 4.6 V during the 1st charge and at 2.5 V at the end of the 1st discharge. The cycling curves obtained are shown in **Figure S8**, **Figure S9** and **Figure S10** respectively for the 870-5-air sample, the 86-PL sample and the 17-PL sample.

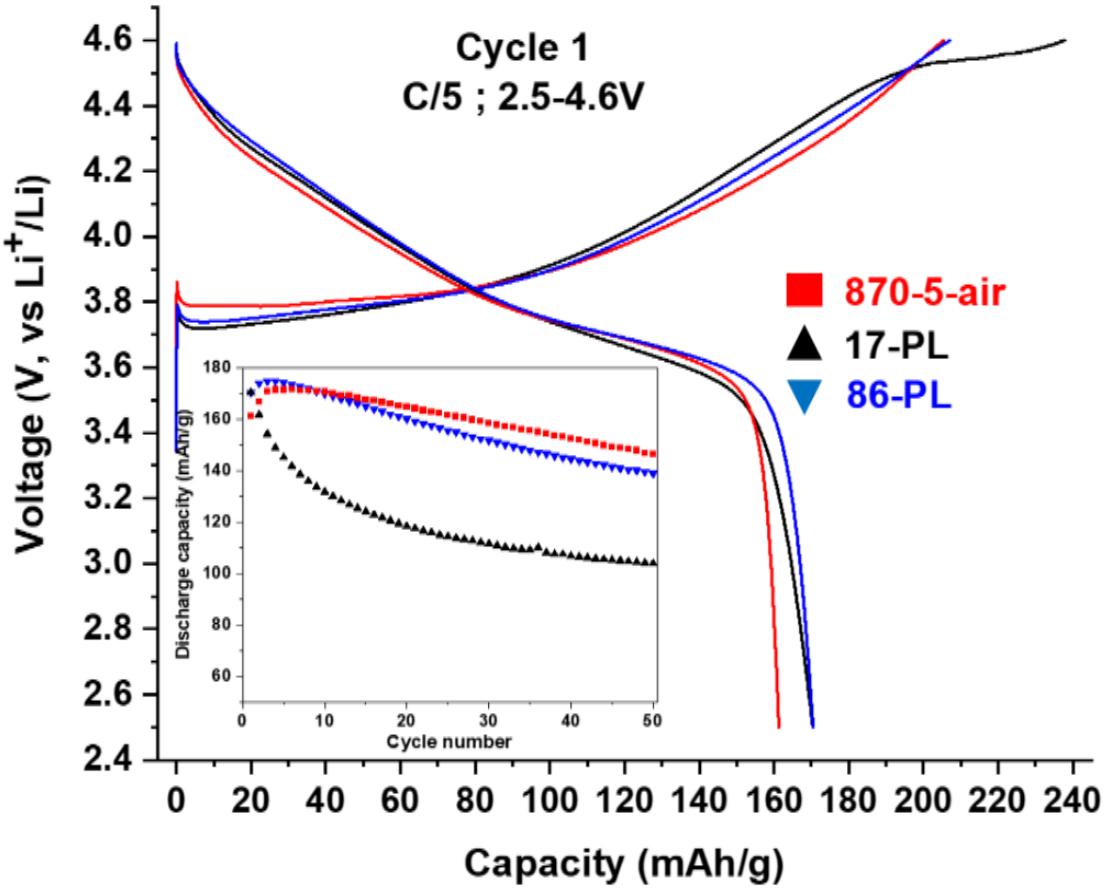

Figure 6. Charge-discharge curves obtained during the 1st cycle for the conventional particles (870-5-air, red line), the 17 nm platelets (17-PL, black line) and the 86 nm platelets (86-PL, blue line) when cycled at C/5 in the 2.5-4.6 V potential range. Evolution of the discharge capacities delivered by the three materials as function of the cycle number (inset) (870-5-air, red squares), (17-PL, black triangles) and (86-PL, blue triangles).

Electrode/electrolyte interface analyses

Cycling was performed in an electrolyte consisting of $LiPF_6$ in a mixture of DMC and FEC. As it was demonstrated that the degradation products of the salt are mostly LiF and $Li_xPF_yO_z$-type species while carbonaceous and oxygenated species are generated from the decomposition of the solvents,[44–50] a particular attention has been paid to contributions

corresponding to these degradation species in the C1s and F1s spectra. The coverage of the active electrode material by these degradation products has been estimated by the analysis of the Li1s, Ni3p, Co3p, Mn3p and O1s XPS spectra. Pristine electrodes and electrodes only exposed to the electrolyte, without any cycling, were also analyzed as references (named as pristine and OCV electrodes hereafter). The F1s and C1s spectra obtained for the three materials at different states of charge and discharge are given in **Figure 7**, whereas the corresponding Li1s, Ni3p, Co3p, Mn3p and O1s XPS spectra are compared in **Figure 8**.

First, we discuss the additional contributions observed in the pristine electrodes. As the binder and the electrolyte contains fluorine species, XPS signal assigned to fluorine element is detected and we are particularly investigating the F1s spectra. They are composed of two contributions, one located at 688.0 eV attributed to the CF_2 environments from the PVDF binder and one contribution at 685.1 eV attributed to LiF, formed in small amount in the case of pristine electrodes by reaction between the fluorine of PVDF and the Li of the active material.[51,52] As for the initial powder, adventitious carbon is always present at the electrode surface (located at 285.0 eV, 286.4 eV, 287.4 eV, 288.8 eV and 290.2 eV for C-C/C-H, -C-O, -C=O, $-CO_2$ and $-CO_3^{2-}$ environments respectively[51,52]). But, new contributions to the C1s spectra appear according to carbonaceous species present in the electrolyte, binder and carbon black. The PVDF binder is associated to two new components located at 286.5 eV ($\underline{\mathbf{C}}H_2$-$CF_2$) and 291.0 eV ($CH_2$-$\underline{\mathbf{C}}F_2$). The signature of the carbon black (B.E. C1s = 284.7 eV) in the electrode is well characterized by a set of black peaks corresponding to the XPS signal of our laboratory reference. The carbonate contribution comes from Li_2CO_3 at the surface of the active material, as already observed for the pristine powders of the three NMC622 samples in **Figure 4**. In the Li1s spectra, components associated to Li in the NMC material at 54.3 eV and the $Li_{Li_2CO_3}$ one at 55.4 eV are always detected. A third component is appearing at 56.3

eV attributed to LiF species in accordance with the contribution observed at 685.1 eV in the F1s spectra. We highlight that a clear decrease of the O_{NMC} contribution at 529.6 eV (from 24 at.% to 10 at.% for the whole O1s signal) due to the presence of oxygenated species coming from the electrode formulation and thus to a partial coverage of the active electrode material. At first, the electrode prepared with platelets material contain, at the surface, more binder and CB that the electrode prepared with the traditional morphology material. Moreover, at the surface of 870-5-air electrode, we note a large content of lithium carbonate, as already detected in the as-prepared material.

After cycling, an evolution in the core peaks spectra is observed. First, we describe the new environment detected by XPS whatever the cycling step. In the F1s spectra, a third component (in dark blue) appears at 686.6 eV associated to the creation of $Li_xPF_yO_z$ species. A huge increase of the LiF component (in dark green) is also observed at the OCV step. Those species coming from the electrolyte salt decomposition induce the increase of the $LiF/Li_xPF_yO_z$ components (in dark green) at 56.2 eV in the Li1s spectra and at 685.6 eV in the F1s spectra. In the O1s spectra, we observe an enlargement of the peak due the apparition of oxygen component (located at 534.4 eV) associated to the fluorophosphates species and a large increase of the component at 532.5 eV associated to the C-O environment of the DMC and FEC solvents.[51,52] The component assigned to the NMC oxygen atoms at 529.6 eV is still present along the first cycle. The area of the peak located at 531.5 eV is increasing as it includes oxygen function linked to solvent degradation like CO_2 or O=C species. In the C1s spectra, the solvents degradation generates a clear increase of the contributions at 285.0 eV, 286.5 eV, 288.9 eV assigned to C-C/C-H, C-O, and CO_2 environments respectively, thus confirming the attributions previously made.

Quantitative analyses were performed to estimate the surface composition of those electrodes as a function of the state of charge in order to study the reactivity of the materials versus the electrolyte depending on their morphology. The results obtained from the quantitative surface analysis of the 870-5-air sample (conventional particles) recovered at 4.3V vs. Li^+/Li at the end of the 1st charge are given in **Table S5** as an example. The overall quantitative analyses are reported in **Table S6, Table S7** and **Table S8** and summarized in **Figure 9** and **Figure S11**, as a comparison of evolution observed for the three NMC622 samples. In those tables and figures, the different components reported in the XPS spectra are gathered into 5 chemical groups in order to follow the electrolyte degradation and the electrode covering during cycling. The quantitative results are obtained as following for: $LiF/Li_xPF_yO_z$ species, sum of the atomic percentages of LiF and $Li_xPF_yO_z$ components from the Li1s, F1s, O1s and P2p spectra; for the active material, sum of the at.% of the Ni, Mn, Co, O_{NMC} and Li_{NMC} components in the O1s and Li1s spectra; for the carbon black (at.% of the as-named components in the C1s spectra); for PVDF, sum of the at.% of the PVDF components in C1s and F1s spectra; and for carbonaceous species, sum of the at.% of the remaining components (other than that of CB and PVDF) in C1s spectra, the remaining contributions in O1s spectra (different from O_{NMC} and phosphate species) and the Li_2CO_3 contribution in Li1s spectra. Only the most relevant values obtained from those quantitative analyses are discussed hereafter.

First, the pristine electrodes are compared to the OCV electrodes. For the two platelets materials, the decrease of carbon black and PVDF contributions after OCV step (from 31.7 at.% to 7.6 at.% and from 27.3 at.% to 12.8 at.% respectively for the 86-PL sample as example) while keeping roughly the same proportion of active material suggests a selective coverage of electrodes surface by the degradation products from the moment they are exposed

to the electrolyte. Especially the important increase of $LiF/Li_xPF_yO_z$ and carbonaceous species proportions (from 2.5 at.% to 15.8 at.% and from 34.0 at.% to 61.0 at.% respectively for the 86-PL sample for example) is in accordance with this observation. On the other hand, to identify a possible diffusion of chemical species especially fluorine within the particle aggregates, AES analyses (**Figure S12**) were performed on a cross cut section of this sample. As shown on **Figure S12a**, AES spectra were recorded on 3 target dots on the material section shown on the SEM image of the **Figure S12b**. Spectra of dot 1 and dot 2 exhibit clearly visible Mn LMM (525-640 eV), Co LMM (620-780 eV) and Ni LMM (675-860 eV) transitions. In comparison, the spectrum of dot 3 targeting the PVDF matrix only displays a F KLL (620-660 eV) transition in the same energy range. For dot 1 and dot 2, due to the overlapping of the metal and fluorine transitions, attesting of the presence of fluorine on the NMC particle aggregates from the direct spectra is difficult. However, it is possible through the derivative experimental spectra of the dots 1 and 2 in **Figure S12c**. Such spectra have been well-fitted by the convolution of MnO, CoO, NiO and LiF reference spectra showing a significant contribution of fluorine in the experimental signals. In addition, Scanning Auger Mapping (SAM) elemental maps of the cross cut section were also obtained (**Figure S12d**). The SAM images, especially the Ni/C overlaid map, show a good junction between the active NMC material and the matrix after cycling. Moreover, a low but significant fluorine detection (in red) on the particles is also displayed on the F map and Ni/F overlaid map in good agreement with the previous observation of AES spectra. For the 870-5-air sample (conventional particles), the electrode surface reactivity is completely different as the at.% of CB and PVDF are not decreasing in the same manner than for the platelets samples. Thus, the degradation products are covering a major part of the active material. Indeed the proportion of PVDF contributions even increases from 14.4 at.% to 24.0 at.% after OCV step reflecting the uncovering of some parts of the electrode. At the same time, a significant decrease of the

carbonaceous species proportion is observed from 50.0 at.% to 25.3 at.% (**Table S6**), reflecting the dissolution of a large amount of carbonaceous impurities at the surface of the electrode, including Li_2CO_3 (from 36.8 to 7.2 at.%) present in large amount at the surface of the 870-5-air sample (conventional particles) as shown previously in **Figure 4.** Then, the surface's composition of electrodes recovered at different states of charge or discharge during the 1st cycle is compared for the three morphologies. A larger amount of LiF/$Li_xPF_yO_z$ species is observed at the surface of the 17 nm thick platelets (17-PL sample) compared to the 2 other morphologies, regardless of the state of charge (**Figure 9a**) (37.6 at.% for the 17-PL sample at 4.6 V for example versus 20.3 at.% for the 86-PL and 23.4 at.% for the 870-5-air): it reveals the more pronounced $LiPF_6$ degradation at the surface of those thin platelets. In good agreement with one of our previous works that studied the reactivity at the surface of NMC622 type samples depending on their particles' size, this would be due to the larger specific surface area observed for the sample made of the thinnest platelets (12 m^2/g vs. less than 4 m^2/g for the others).[53]

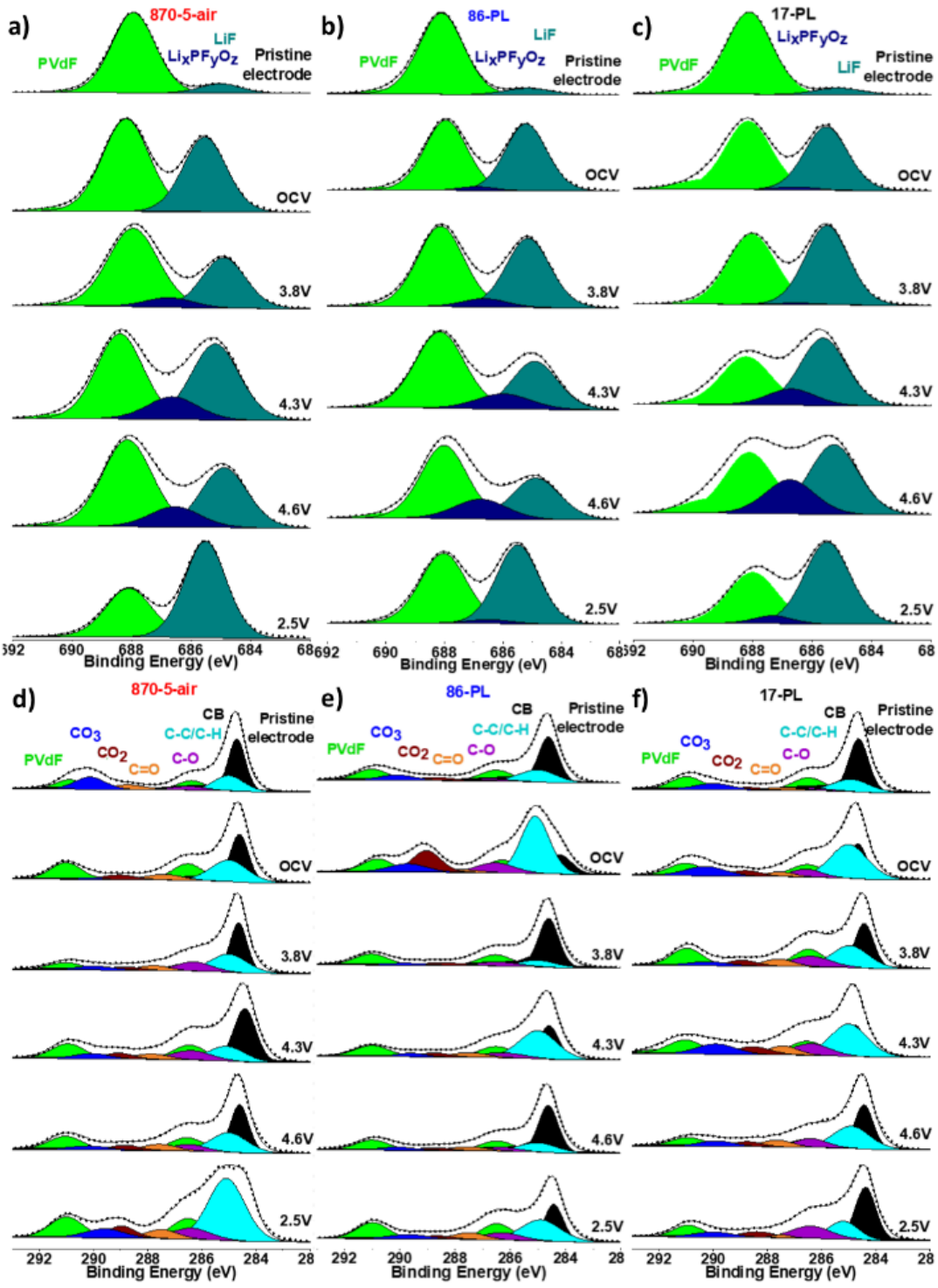

Figure 7. F1s (a-c) and C1s spectra (d-f) obtained from XPS analyses of the 870-5-air sample (conventional particles) (a, d), the 86-PL sample (86 nm thick platelets) (b, e) and the 17-PL sample (17 nm thick platelets) (c, f) after their cycling versus Li metal. The dots and the lines represent the experimental and the fitted data respectively.

More carbonaceous species are found at the surface of the conventional particles at the end of discharge (38.2 at.% for the 870-5-air sample at 2.5 V versus 25.6 at.% and 22.3 at.% for the 17-PL and 86-PL samples, as shown in **Figure 9b**) while more similar amounts are found at the end of charge for the three morphologies, so the solvents (here DMC and FEC) would be more degraded in contact with conventional particles in discharge. Regarding the amount of carbon black observed at the surface of the electrodes after cycling, it is found to decrease significantly for 86-PL and 870-5-air at almost every state of charge whereas it is maintained constant, but at a lower level, for 17-PL (12.3 at.% for the 17-PL sample at 4.6 V for example versus 28.8 at.% for the 86-PL sample and 17.5 at.% for the 870-5-air sample, as shown in **Figure 9c**). The cycling does not modify the amount of PVDF observed at the surface of the electrodes after the OCV step (as shown in **Figure S11a**, 13.9 at.% for the 17-PL sample at 4.6 V for example versus 22.5 at.% for the 86-PL sample and 21.2 at.% for the 870-5-air sample).

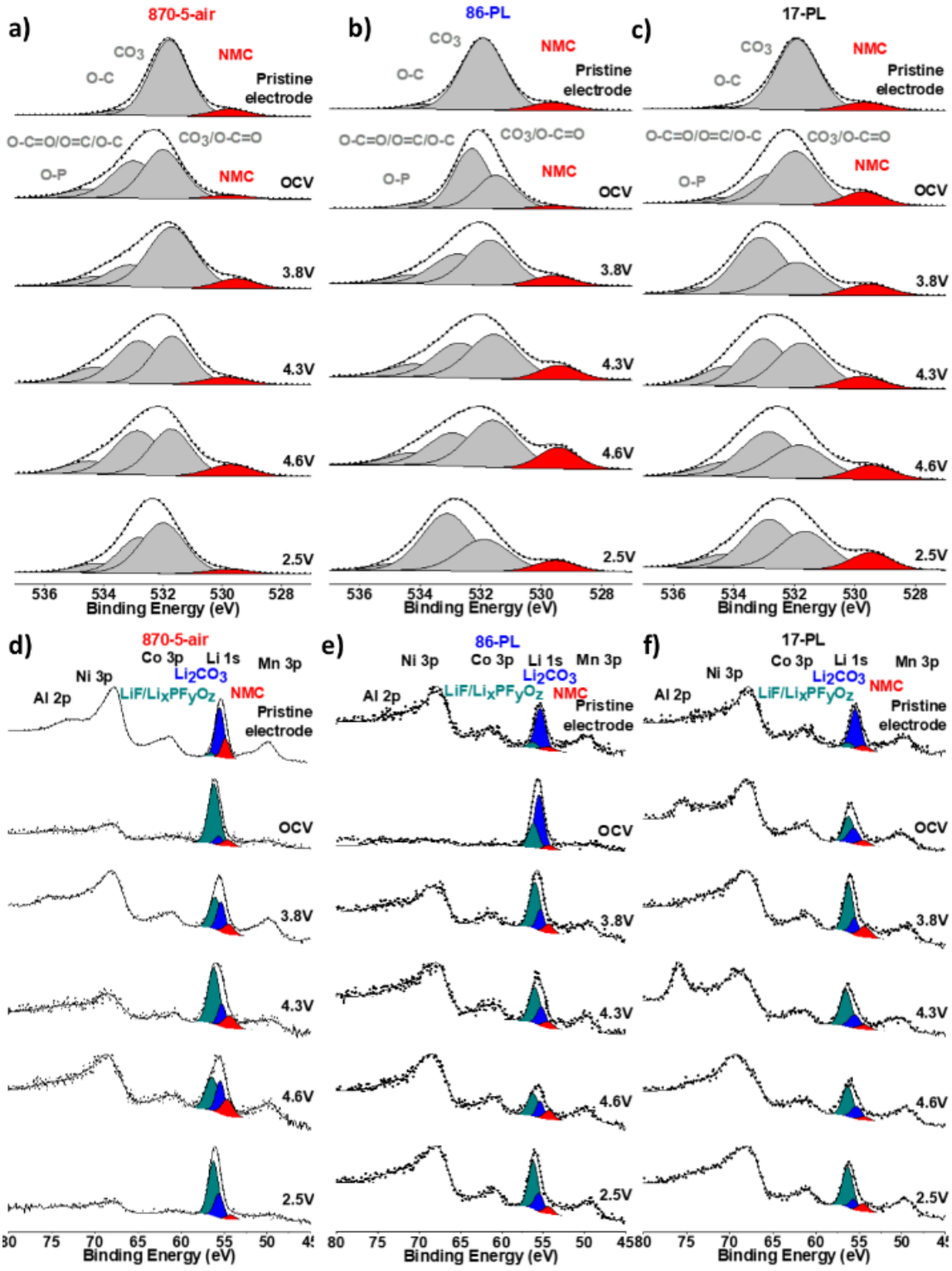

Figure 8. O1s (a-c) as well as Li1s, Ni3p, Co3p and Mn3p spectra (d-f) obtained from XPS analyses of the 870-5-air sample (conventional particles) (a, d), the 86-PL sample (86 nm thick platelets) (b, e) and the 17-PL sample (17 nm thick platelets) (c, f) after their cycling

versus Li metal. The dots and the lines represent the experimental and the fitted data respectively.

Both observations made for carbon black and PVDF suggest a larger coverage of the 17-PL electrodes by a layer built from the electrolyte degradation from the OCV step. The coverage results from two antagonist phenomena observed in parallel: the dissolution of Li_2CO_3 present at the surface of the pristine NMC in the electrolyte and the formation of a SEI layer at the surface of the cycled electrodes upon cycling (**Figure S11b**). For the particles having a large amount of Li_2CO_3 at their surface, like the conventional ones, the two phenomena, occurring simultaneously, lead to a fluctuant evolution of the covering at the beginning of cycling, until the formation of SEI becomes predominant and induces a pronounced increase of the particles covering. In the case of the 17-PL sample, with a lower amount of Li_2CO_3 at its surface, the dissolution of Li_2CO_3 is less pronounced, leading to a more monotonous evolution of the covering due to the formation of SEI. Depending on the morphology of the particles and the nature of the facets exposed, the nature and amount of degradation products is different from one sample to another. Regarding the amount of degradation products, these results showed that a larger amount of degradation products were formed at the surface of the 17 nm platelets (17-PL sample). Regarding the nature of those degradation products, these results reflect an exacerbated degradation of the salt $LiPF_6$ at the surface of the 17 nm thick platelets (17-PL sample), suggesting a much more pronounced reactivity of the {001} facets (those of the platelets) versus the lithium salt, which generates a SEI layer richer in lithium salt degradation products at the electrode/electrolyte interface.

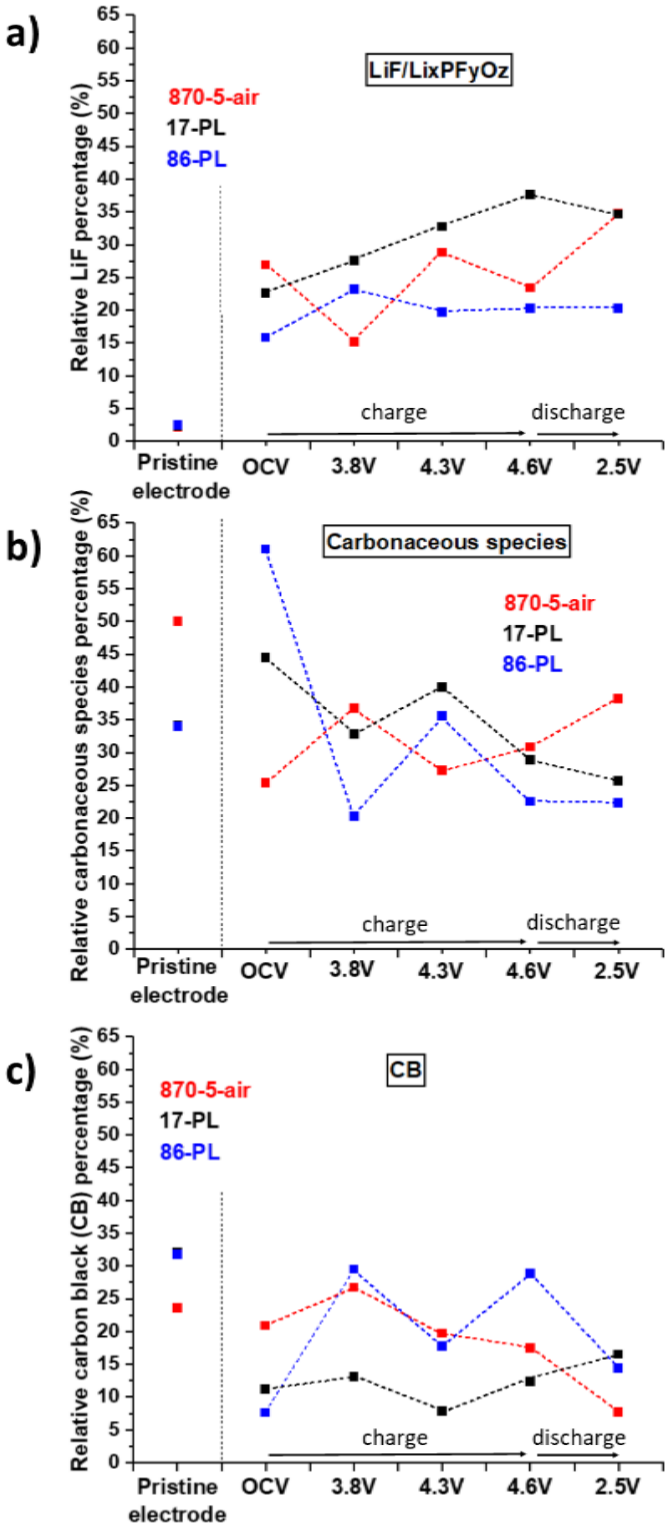

Figure 9. $LiF/Li_xPF_yO_z$ species (a), carbonaceous species (b) and carbon black (c) surface proportions obtained from the XPS quantitative analyses performed on the 870-5-air (conventional particles), the 86-PL (86 nm thick platelets) and the 17-PL (17 nm thick platelets) cycled electrodes.

Those results also show that the exposition of larger {010} facets by increasing the thickness of the platelets, enables to minimize the proportion of {001} facets leading to a lower reactivity of the material versus the lithium salt and the solvents, so a lower amount of degradation products is generated at the electrode/electrolyte interface compared to the 17 nm platelets and the conventional particles. We can also conclude that the SEI is less than 10 nm thick or does not cover completely the surface as XPS signal associated to NMC material is still detectable at the end of the 1st cycle.

Structural analysis after cycling

XRD analysis was also performed *ex situ* on electrodes recovered after cycling at the same states of charge during the 1st cycle to compare the structural changes occurring for the three samples. The XRD patterns collected for the 870-5-air sample (with conventional particles), the 86-PL sample (86 nm thick platelets) and the 17-PL (17 nm thick platelets) are gathered in **Figure S13**, **Figure S14** and **Figure S15** respectively. If no particular evolution, versus those already reported in literature for NMC622 type layered oxides, is observed for the conventional particles (870-5-air) and the 86 nm thick platelets (86-PL), additional reflections clearly appear at the end of charge for the 17 nm thick platelets (17-PL) at 19.9°, 41.8° and 55.4°(2θ) (**Figure S15**). **Figure 10a-c** focus on the 17-21°(2θ) angular range where the diffraction lines corresponding to the c_{hex} parameter are observed. Indeed, this cell parameter is very sensitive to structural variations occurring during cycling, as the amount of Li^+ ions present within the structure controls changes in the iono-covalency of the M-O bonds in the MO_2 slabs and the electrostatic repulsions between the oxygen layers from both sides of the interslab spaces.[54,55] As reported in literature,[43,56–59] during delithiation the layered oxide NMC622 undergoes structural changes with first the pristine phase H1 for compositions in Li

richer than 0.6 and whose structures are described in the *R-3m* space group, then the phase H2 isostructural to H1 but with a smaller $a_{hex.}$ parameter and a larger $c_{hex.}$ parameter, and finally for lithium content lower than 0.3 the phase H3 isostructural to H1 and H2 but with an even smaller $a_{hex.}$ parameter and a contracted $c_{hex.}$ parameter. The $a_{hex.}$ parameter decreases continuously all along Li^+ deintercalation as the transition metal ions are oxidized leading to a higher covalency of the M-O bonds and thus to a decrease of the M-M (= a_{hex}) distance. The $c_{hex.}$ parameter is the sum of the slab and interslab thicknesses, the first decreases continuously upon Li^+ deintercalation as the M-O bond becomes more covalent and thus shorter, and the second increases first due to the electrostatic repulsions between the oxygen layers before decreasing due a higher covalency of the M-O bonds and thus a lower negative partial charge on the oxygen anions. The $c_{hex.}$ parameter thus increases first before decreasing.

The phase diagram and crystallographic parameters of the phases identified at each state of charge or discharge were determined from Le Bail refinements of all the XRD data collected *ex situ*. The evolution of the $c_{hex.}$ parameter as function of the content in lithium is illustrated in **Figure 11**, the Li content being that associated to the electrochemical experiment and to the number of electrons exchanged. For the materials obtained at 3.8 and 4.3 V (lithium content in the range of about 0.8 to 0.3), whatever the morphology of the layered oxide NMC622, two phases are needed to refine the XRD data. The coexistence of the H1 and H2 phases can be deduced from the chex. values, of 14.16-14.22 and 14.30-14.36 Å for H1 and H2 respectively. For the electrode materials recovered at 4.6 V, one H2 phase is needed for the 870-5-air while two and three phases are needed to explain the XRD data of the 86-PL and the 17-PL material respectively (**Figure 10d-f**). The new phase, denoted H4, has a much smaller $c_{hex.}$ parameter of 13.40 Å compared to 13.79 Å for the H3 phase. This type of phase was already observed for the close-to-the-stoichiometry $LiNiO_2$ and appears only when the amount of Li and extra

Ni ions present in the Li site is low as the formation of the phase H4 requires slab gliding to stabilize an AB AB type oxygen packing (S.G *P-3m1*) from the AB CA BC one observed for H1, H2 and H3, as described in **Figure 11**.[58,59] The diffraction lines broadening observed, especially at high voltage, in comparison with that of the pristine XRD can be explained by the presence of 2 or 3 layered phases at the same time within the particles. These particles are intergrowths of domains of limited sizes showing different Li contents and possibly stacking (O3 vs O1). As highlighted in **Figures S14-S15**, these phase transitions are reversible, with values of c_{hex} parameter obtained at end of discharge between 14.10 Å and 14.21 Å, close to the ones obtained for the pristine electrodes between 14.21 Å and 14.23 Å (see **Figure 11**).

The 17 nm thick platelets with less than 2.7% Ni^{2+} ions in excess in the Li sites as determined by Rietveld refinement (**Table 1)** are prone to favor easier Li^{+} ions diffusion and formation of highly deintercalated compositions, and thus stabilization of the phase H4 with an O1-type stacking. The more drastic c_{hex} parameter drop is observed for the 17 nm thick platelets (17-PL), versus that observed for the 86 nm thick platelets (86-PL), with the apparition of the H4 phase: it can be partly explained by the lower amount of Ni^{2+} ions present in the Li sites, i.e. 2.7% for 17-PL versus 5.2% for 86-PL as determined by Rietveld refinement (**Table 1**). Indeed, the Ni ions present in the interslab spaces play the role of pillars preventing the collapse of the interslab space and the slab gliding required to form the O1 stacking from the O3 one.[59] However, it is worth mentioning that the conventional particles with only 3.4% Ni ions in excess in the Li sites, versus 5.2% in the 86 nm thick platelets (86-PL), reveal limited Li deintercalation ratio: at the end of the charge only the phase H2 is observed whereas H3 and/or H4 are observed for the platelets morphologies, inferring that the morphology plays a significant role.

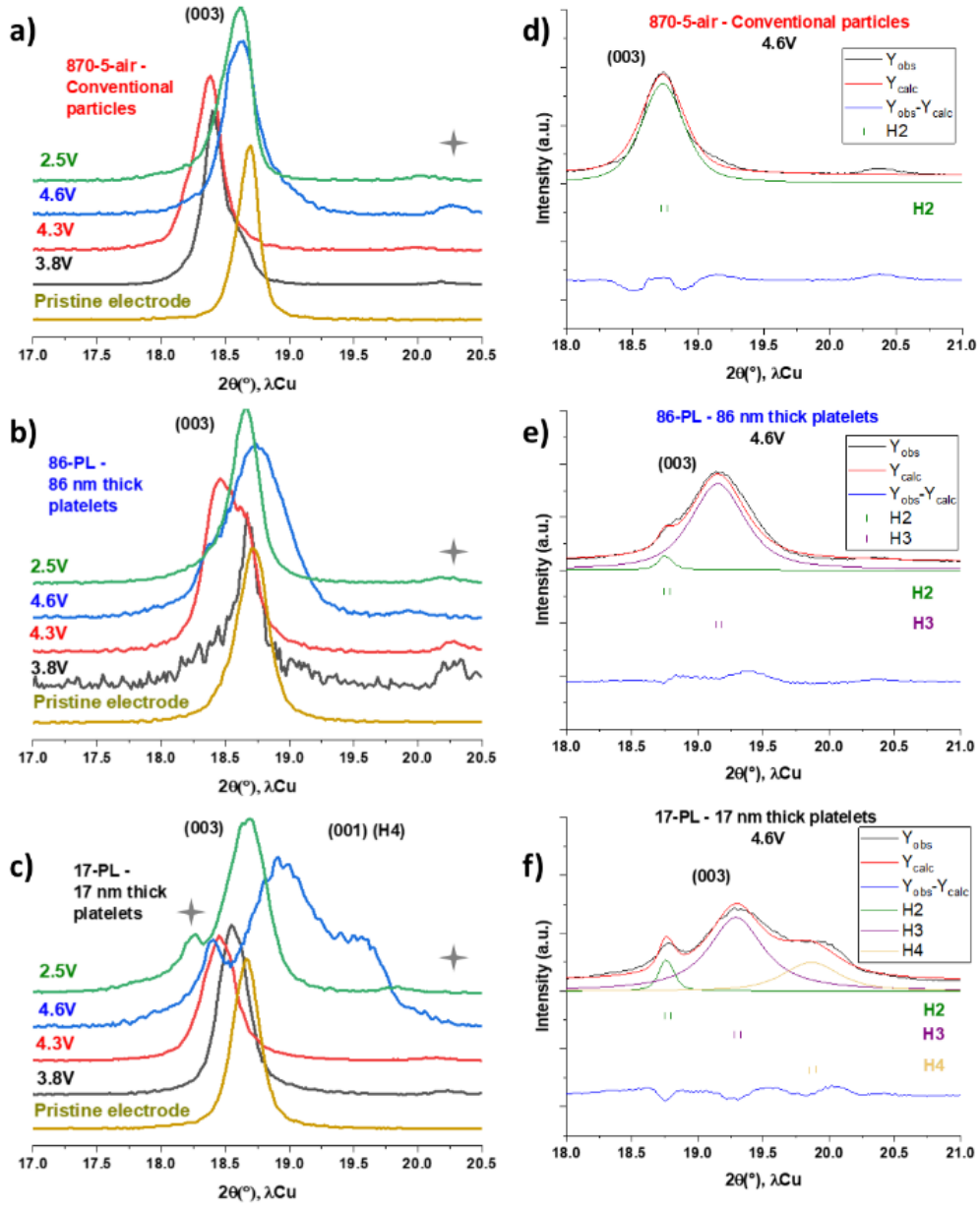

Figure 10. (003) peak evolution obtained from the XRD patterns of the 870-5-air (conventional particles) (a), 86-PL (86 nm thick platelets) (b), and 17-PL (17 nm thick platelets) (c) cycled electrodes. Le Bail refinement and phase identification carried out on the XRD patterns collected for electrodes recovered at 4.6 V vs. Li^+/Li for the 870-5-air (with conventional particles) (d), 86-PL (with 86 nm thick platelets) (e) and 17-PL (with 17 nm thick platelets) (f) samples. The peaks emphasized by the grey stars are small contributions coming from the sample holder.

Those results show that the platelet morphology promotes phase transitions causing anisotropic volume changes. Those structural changes happening during cycling were known to be dependent on NMC composition and on the cut-off voltage. At higher Ni content (in $Li(Ni_xMn_{1-x}Co_{1-x})O_2$, $x > 0.6$), the H2→H3 phase transition can be observed at lower cut-off potentials, at around 4.2-4.3V for the $Li(Ni_xMn_{1-x}Co_{1-x})O_2$ compounds with $x \geq 0.8$.[2,56,57] These results show that those phase transitions are also dependent on the morphology.

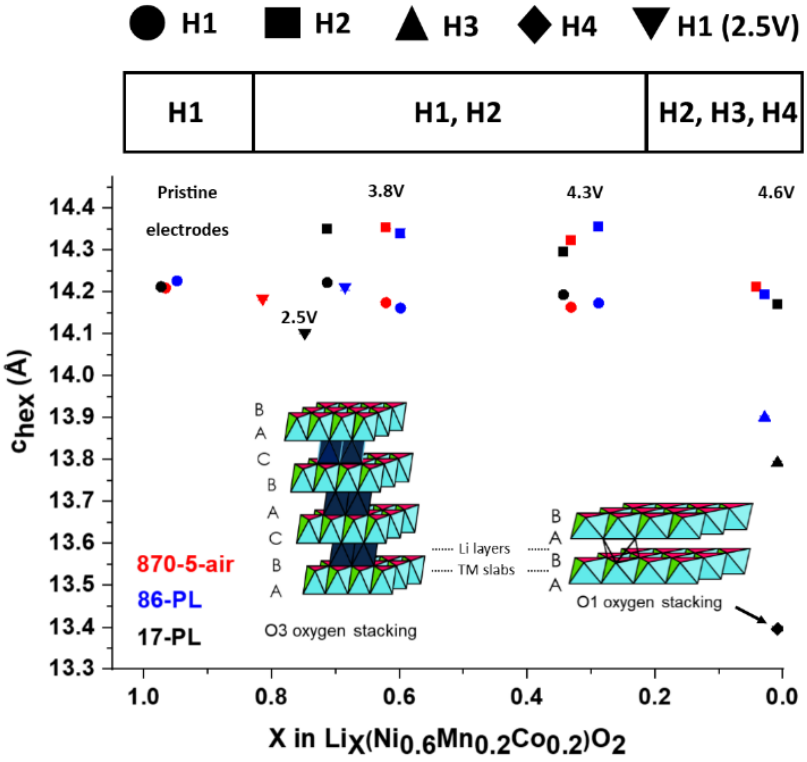

Figure 11. Evolution of the chex parameter as a function of the Li content in the layered oxide Li_XMO_2 for the conventional particles (870-5-air, in red), the 17 nm thick platelets (17-PL, in black) and the 86 nm thick platelets (86-PL, in blue). The results are given for the pristine electrode (X≈1 depending on the amount of Ni ions in Li site as determined by Rietveld refinement) and the electrodes cycled and stopped at 3.8 V, 4.3 V, 4.6 V and 2.5 V. O3 oxygen stacking associated to H1, H2 and H3 phases and O1 oxygen stacking associated to the H4 phase are also displayed.

Discussion

Three NMC622 layered oxides with different morphologies were studied in this work: one sample with 280 nm primary particles of conventional morphology and two other samples with platelet-shaped particles of 17 nm and 86 nm thickness. The three materials have a layered structure close to the ideal 2D layered structure, with less than 5.2% Ni^{2+} ions in the Li site and the desired composition in transition metals and lithium, both in the bulk and at the surface. Only differences in surface composition were observed with lower amounts of Li_2CO_3 at the surface of the platelets thanks to a higher proportion of less reactive surfaces to ambient air (see **Figure 4**). The three materials are then very similar in structure and in chemical composition, their main difference being their morphology. Cycling tests were performed on those three materials to investigate the influence of these different morphologies on the electrochemical performances. The results obtained from the analyses performed after cycling up to 4.6V in GITT conditions helped us to explain the electrochemical performances observed.

Phase transitions and surface composition depending on the delithiation rate/potential

For cyclings performed at different rates from C/10 to 2C in the 2.5-4.3 V potential window, the 17 nm platelets showed slightly better performances than the two other morphologies but the difference with the performances of the conventional particles was not significant, especially at high rates (see **Figure 5**). In the 2.5-4.3 V potential window, moderate delithiation ratios ($X \approx 0.34$-0.38 in $Li_X(Ni_{0.6}Mn_{0.2}Co_{0.2})O_2$ at C/10 at 1st cycle, see **Figure S5b**) are reached so no significant structural changes are expected to occur in the materials and, as observed in the electrochemical tests, no significant capacity loss was observed for the

three materials, whatever the cycling rates. Cyclings were also performed in a larger potential window (2.5-4.6 V) at C/5 to study the behaviour of those materials when reaching higher delithiation ratios (X ≈ 0.15-0.26 in $Li_X(Ni_{0.6}Mn_{0.2}Co_{0.2})O_2$ at C/5 at 1st cycle, see **Figure S6b**) that may be critical for the stability of the material during cycling. Indeed, at such potential/delithiation ratios, phase transitions in the layered phase domain such as H2→H3 are known to be harmful for the structure and the cyclability of the material because of pronounced c_{hex} parameter drop.[43,56–59] In those cycling conditions, as observed in **Figure 6** and **Table 2**, the platelets showed higher 1st discharge capacities than the conventional particles but the 17 nm platelets showed very reduced capacity retention caused by an irreversible oxidation occurring at the end of the 1st charge between 4.5 and 4.6 V. The 86 nm platelets and the conventional particles showed similar capacity retentions. As shown in **Figures S8-S10**, higher delithiation ratios are reached in GITT conditions at end of charge ($X \approx 0$ in $Li_X(Ni_{0.6}Mn_{0.2}Co_{0.2})O_2$, some of them even going slightly into negative values because of the degradation of the electrolyte). As a consequence, and as shown in **Figure 10** and **Figure 11**, H2→H3 and even H3→H4 phase transitions occur causing large anisotropic volume changes, that would induce strains and a loss of percolation in the material. This causes a significant reduction of the performances along cycling. Those phase transitions are clearly enhanced by the platelet morphology because of their orientation that enhances the diffusion of Li^+ ions into the structure and the structural collapse at the particle level when high delithiation rates are reached. Regarding the XPS experiments, the large amount of $LiF/Li_xPF_yO_z$ species at the surface of the 17 nm platelets at all the states of charge studied revealed an exacerbated reactivity of the lithium salt $LiPF_6$ versus the {001} facets that are extended versus other crystallographic orientations in this material. On the contrary, the slightly lower amount of degradation products at the surface of the 86 nm platelets showed a reduced reactivity induced by the increase of the proportion of {010} facets in the material.

Relation between the phase transitions and the surface composition

The more intense volume changes observed for the 17 nm thick platelets (17-PL) as well as the larger amount of $LiF/Li_xPF_yO_z$ resistive species found at their surface must explain the lower capacity retention observed for the 17 nm platelets (17-PL) when cycled at C/5 in the 2.5-4.6 V potential window (**Figure 6**). Contrary to the GITT experiments, the H3→H4 phase transition is not expected to intervene in the C/5 cycling conditions because the delithiation ratios reached are not high enough to allow such phase transition.[58,59] However, the H2→H3 phase transition is very likely to occur, concomitantly with oxygen release due to the stabilization of the M^{4+} ions into M^{2+} ions.[43] This oxygen release would be limited to the near-surface region because of the limited diffusion length of oxygen anions in NMC particles at 25°C.[43] This could be associated to the irreversible oxidation observed for the 17 nm platelets at end of charge in **Figure 6** and **Figure S6**. As the surface area is 3 times larger for the 17 nm thick platelets (17-PL) than for the 86 nm thick platelets (86-PL), it would explain why this surface phenomenon is significantly observed only for the 17 nm thick platelets (17-PL) in the C/5 cycling. This oxygen loss in the near-surface region inevitably accompanies with the transformation of the layered structure to spinel and/or rocksalt structure, although those phases were not observed on the XRD patterns obtained after cycling, since they must be limited to a few atomic layers. As this layer forms, the amount of oxygen released decreases because of the limited diffusivity of oxygen anions in the lattice, the oxygen-depleted surface layer gradually stops forming and the active material/electrolyte interface stabilizes. As observed with the evolution of the dQ/dV curves of the 17-PL sample (17 nm platelets) for the C/5 cycling in **Figure S7**, the irreversible oxidation occurs mainly at 1st cycle as the oxidation peak at 4.5-4.6 V disappears almost completely from the 2nd cycle. This release of reactive oxygen may also be responsible for a more important degradation of the electrolyte

by electrochemical oxidation.[43] This degradation would create a large amount of degradation products and the lower surface energy of the {001} facets would allow the deposition of those products and facilitate their adsorption at their surface, like it does for specific solvents.[13,18,22,60] This would explain the more important covering of the 17-PL (17 nm platelets) electrodes by the SEI, as shown in **Figure 9**. Moreover, a quick increase of the internal resistance is observed from the shift of the potential at the beginning of discharge reflecting the formation of a resistive surface layer that hinders the reintercalation of Li ions into the structure. This internal resistance increases quickly during the first cycles and less rapidly in the following cycles. Similarly, as observed in **Figure 6**, the capacity drop of the 17 nm platelets (17-PL) is very fast during the 10 first cycles and less rapid afterwards, reflecting a stabilization of the surface of the material.

Stability of the different facets during cycling

Those results infer that the 17 nm platelets (17-PL), with extended {001} facets, are more prone to undergo phase transitions and associated oxygen loss during cycling. This is in opposition with what was shown by Jung et al.[61] They studied doped $LiNi_{0.92}Mn_{0.04}Co_{0.04}O_2$ platelet-shaped particles of different thicknesses, boron-doped particles of 74 nm thickness and phosphorus-doped particles of 144 nm thickness in average, and they showed that the 144 nm platelets were more prone to oxygen loss and phase transition during cycling compared to the thinnest ones.[61] From first-principle calculations, they revealed that the (102) planes, identified as the lateral planes of their particles, were more prone to undergo oxygen release compared to the (003) planes due to a lower oxygen vacancy formation energy.[61] However, they also showed that doping had modified the surface composition of their particles and made them less prone to oxygen loss, so the reactivity of the facets was very likely modified

by the doping. Zhu and Chen studied NMC333 materials with different morphologies.[13] They compared platelet-like particles with extended {001} surfaces being ~100 nm thick and polyhedral particles of ~100 nm with a majority of {012} (lateral) surfaces. Despite the larger capacities delivered by the polyhedral particles, thanks to the more opened Li^+ ion diffusion pathways, they also emphasized the higher stability of the platelet-like particles with extended {001} facets, due to their lower surface energy making them less prone to Ni surface reduction, less reactive and more stable during electrochemical cycling.[13] However, in that case, their particles are closer to the morphology obtained for our 86 nm platelets and conventional particles, that showed to be more stable than our 17 nm platelets. Our 17 nm platelets, showing the most unstable behaviour during cycling, are mainly composed of {001} facets that are supposed to be among the most stable during cycling. The main difference between our samples and the ones described in these articles is that, our 17 nm platelets are much thinner so they generate a much larger amount of surfaces, as shown by the BET surface area measurements given in **Figure 2**. As the oxygen release phenomenon is observed at the surface, it could explain why oxygen release is more intense for this morphology despite the relative stability of the {001} facets compared to the others. The larger specific surface area may play a significant role here and must explain the relative instability of the 17 nm platelets compared to thicker platelets.

Strategies to overcome the exacerbated reactivity of the thin platelets

Increasing the thickness of the platelets to some extent, up to around 100 nm for example, may allow to alleviate the high reactivity of the thin platelets morphology without exposing a too large amount of lateral facets that were shown to be more reactive than the {001}.[13,61] Another efficient way could be also to increase the length of the platelets and to organize

them radially into the agglomerates. Du et al. synthesized such NMC 811 particles organized radially into the secondary particles and revealed the important role played by the particles dimension and organization in the H2→H3 phase transition at end of charge.[16] This strategy allowed them to obtain slightly better capacities compared to randomly distributed particles with a 1st discharge capacity of 222 mAh/g (versus 213 mAh/g for the randomly distributed particles) when cycling at C/5 in the 2.8-4.6 V potential window, their radially grown platelet-like particles giving the Li^+ ions ideally oriented pathways. They showed that long radially-oriented platelet-like particles allowed to have gradually distributed Li^+ ions inside the diffusion channels, acting like a buffer at deep lithiation states, and thus delaying the H2→H3 phase transition. This distribution alleviates the decrease of the c_{hex} parameter, impedes the structure collapse at the particle level and the generation of important volume variations and microstresses caused by this phase transition occurring at deep delithiation state. This particular morphology allowed the particles to deliver slightly improved capacity retention with 85% (versus 82% for the randomly distributed particles) after 150 cycles at C/5 and 76% (versus 70%) after 200 cycles at 1C in the 2.8-4.6 V potential window.[16]

Those results show that platelets dimensions must be chosen carefully because they can have a strong impact on the electrochemical performances and the cycling stability. For cycling at regular potentials such as 4.3 V, thin platelets of 17 nm thickness and thicker platelets of 86 nm thickness can be used because no critical delithiation ratios are reached at this potential in regular cycling conditions. At higher potentials such as 4.6 V, thicker and longer platelets must be preferred in order to improve the structural stability of the particles upon cycling.

CONCLUSION

NMC622 samples with platelet-shaped particles were synthesized by NH_4OH-assisted coprecipitation of a mixed transition metal hydroxide precursor followed by a solid-state reaction with Li_2CO_3 at high temperature. Two samples with crystallographic structure close to the ideal 2D layered structure (less than 5.2% Ni^{2+} ions in Li^+ sites) and with platelet-shaped particles of 86 and 17 nm thickness were obtained. Those two samples were compared to a sample consisting of 280 nm particles with a regular morphology. Unexpectedly, the platelets didn't show better electrochemical performances than the conventional particles, the random orientation of the platelets in large micrometric agglomerates limiting the beneficial effect of oriented particles on the diffusion of Li^+ ions in the structure. The 17 nm platelets showed particular reactivity when cycled up to 4.6 V, with an irreversible oxidation occurring at end of the 1st charge. GITT experiments and post cycling analyses were performed in order to explain this phenomenon. XPS analyses revealed an exacerbated degradation of the electrolyte salt versus the 17 nm platelets leading to a more important covering of the electrodes by the SEI. *Ex situ* XRD analyses after cycling revealed that the H2→H3 and H3→H4 phase transitions were favored at end of charge for the platelets because their crystallographic oriented growth enhances the Li^+ ions diffusion into the structure. Those structural changes are promoted when the platelet is thinner and are responsible for numerous anisotropic volume changes, causing lower capacity retention when cycling is performed at high potential. The smaller dimensions of the 17 nm platelets are also likely to enhance lattice oxygen release at the surface of the particles, which catalyzes the degradation of the electrolyte and explains the larger amount of degradation products found at the surface of the particles.

ASSOCIATED CONTENT

Supporting information

The Supporting information contains Figures, Tables and description to complete and precise some points in the main manuscript, such as: chemical analyses performed by ICP-OES; the synthesis description and characterization of the hydroxide precursors used to obtain the different lithiated layered oxides; the XRD patterns and SEM images obtained for a series of lithiated layered oxides prepared in different synthesis conditions from the hydroxide precursor showing a platelet morphology; as an example, the results of the Rietveld refinements carried out for the XRD and neutron diffraction patterns of one of the studied lithiated layered oxides; the distribution of the platelet lengths in two of the lithiated layered oxides; detailed XPS results (identifications and quantifications); AES analyses, and comparison of the XRD patterns obtained for electrodes recovered after cycling. This material is available free of charge via the Internet at http://pubs.acs.org.

AUTHOR INFORMATION

Corresponding author

* Laurence Croguennec

Laurence.Croguennec@cnrs.fr

* François Weill

François.Weill@cnrs.fr

Funding Sources

This work was funded by Saft and Région Nouvelle Aquitaine.

ACKNOWLEDGEMENTS

The authors acknowledge Saft and Région Nouvelle-Aquitaine for the funding of the project, as well as the French National Research Agency (STORE-EX Labex Project ANR-10-LABX-76-01) for financial support for their research on the electrochemical energy storage. The authors thank Cathy Denage and Eric Lebraud at ICMCB for their technical support for ICP-OES and XRD, respectively. The authors also thank Philippe Legros at PLACAMAT and Marie-Anne Dourges at ISM for their scientific support with SEM and BET analyses.

REFERENCES

(1) Tsiropoulos, I.; Tarvydas, D.; Lebedeva, N. *Li-Ion Batteries for Mobility and Stationary Storage Applications: Scenarios for Costs and Market Growth.*; EU Publications; Publications Office: Luxembourg, **2018**.

(2) Noh, H.-J.; Youn, S.; Yoon, C. S.; Sun, Y.-K. Comparison of the Structural and Electrochemical Properties of Layered $Li[Ni_xCo_yMn_z]O_2$ (x=1/3, 0.5, 0.6, 0.7, 0.8 and 0.85) Cathode Material for Lithium-Ion Batteries. *J. Power Sources* **2013**, *233*, 121-130.

(3) Liang, L.; Du, K.; Peng, Z.; Cao, Y.; Duan, J.; Jiang, J.; Hu, G. Co-Precipitation Synthesis of $Ni_{0.6}Co_{0.2}Mn_{0.2}(OH)_2$ Precursor and Characterization of $LiNi_{0.6}Co_{0.2}Mn_{0.2}O_2$ Cathode Material for Secondary Lithium Batteries. *Electrochim. Acta* **2014**, *130*, 82-89.

(4) Zybert, M.; Ronduda, H.; Szczęsna, A.; Trzeciak, T.; Ostrowski, A.; Żero, E.; Wieczorek, W.; Raróg-Pilecka, W.; Marcinek, M. Different Strategies of Introduction of Lithium Ions into Nickel- manganese- cobalt Carbonate Resulting in $LiNi_{0.6}Mn_{0.2}Co_{0.2}O_2$ (NMC622) Cathode Material for Li-Ion Batteries. *Solid State Ionics* **2020**, *348*, 115273.

(5) Ma, Y.; Li, L.; Wang, L.; Luo, R.; Xu, S.; Wu, F.; Chen, R. Effect of Metal Ion Concentration in Precursor Solution on Structure and Electrochemical Performance of $LiNi_{0.6}Co_{0.2}Mn_{0.2}O_2$. *J. Alloys Compd.* **2019**, *778*, 643-651.

(6) Li, F.; Liu, Z.; Shen, J.; Xu, X.; Zeng, L.; Li, Y.; Zhang, D.; Zuo, S.; Liu, J. Ni-Rich Layered Oxide with Preferred Orientation (110) Plane as a Stable Cathode Material for High-Energy Lithium-Ion Batteries. *Nanomaterials* **2020**, *10* (12), 2495.

(7) Ronduda, H.; Zybert, M.; Szczęsna-Chrzan, A.; Trzeciak, T.; Ostrowski, A.; Szymański, D.; Wieczorek, W.; Raróg-Pilecka, W.; Marcinek, M. On the Sensitivity of the Ni-Rich Layered Cathode Materials for Li-Ion Batteries to the Different Calcination Conditions. *Nanomaterials* **2020**, *10* (10), 2018.

(8) Wang, L.; Wu, B.; Mu, D.; Liu, X.; Peng, Y.; Xu, H.; Liu, Q.; Gai, L.; Wu, F. Single-Crystal $LiNi_{0.6}Co_{0.2}Mn_{0.2}O_2$ as High Performance Cathode Materials for Li-Ion Batteries. *J. Alloys Compd.* **2016**, *674*, 360-367.

(9) Xia, Y.-F.; Nie, M.; Wang, Z.-B.; Yu, F.-D.; Zhang, Y.; Zheng, L.-L.; Wu, J.; Ke, K. Structural, Morphological and Electrochemical Investigation of $LiNi_{0.6}Co_{0.2}Mn_{0.2}O_2$ Cathode Material Synthesized in Different Sintering Conditions. *Ceram. Int.* **2015**, *41* (9), 11815-11823.

(10) Li, H.; Li, J.; Ma, X.; Dahn, J. R. Synthesis of Single Crystal $LiNi_{0.6}Mn_{0.2}Co_{0.2}O_2$ with Enhanced Electrochemical Performance for Lithium Ion Batteries. *J. Electrochem. Soc.* **2018**, *165* (5), A1038-A1045.

(11) Ju, X.; Huang, H.; He, W.; Zheng, H.; Deng, P.; Li, S.; Qu, B.; Wang, T. Surfactant-Assisted Synthesis of High Energy {010} Facets Beneficial to Li-Ion Transport Kinetics with Layered $LiNi_{0.6}Co_{0.2}Mn_{0.2}O_2$. *ACS Sustainable Chem. Eng.* **2018**, *6* (5), 6312-6320.

(12) Jiang, M.; Zhang, Q.; Wu, X.; Chen, Z.; Danilov, D. L.; Eichel, R.-A.; Notten, P. H. L. Synthesis of Ni-Rich Layered-Oxide Nanomaterials with Enhanced Li-Ion Diffusion Pathways as High-Rate Cathodes for Li-Ion Batteries. *ACS Appl. Energy Mater.* **2020**, *3* (7), 6583-6590.

(13) Zhu, J.; Chen, G. Single-Crystal Based Studies for Correlating the Properties and High-Voltage Performance of $Li[Ni_xMn_yCo_{1-x-y}]O_2$ Cathodes. *J. Mater. Chem. A* **2019**, *7* (10), 5463-5474.

(14) Li, J.; Liu, M.; An, J.; Tian, P.; Tang, C.; Jia, T.; Butt, F. K.; Yu, D.; Bai, W.; Cao, C.; Feng, X. The Synergism of Nanoplates with Habit-Tuned Crystal and Substitution of Cobalt with Titanium in Ni-Rich $LiNi_{0.80}Co_{0.15}Al_{0.05}O_2$ Cathode for Lithium-Ion Batteries. *J. Alloys Compd.* **2020**, *829*, 154555.

(15) Zuo, Y.; Xu, G.; Yin, Q.; Sun, Y.; Huang, B.; Liang, G. Hydrothermal Synthesized Rugby–like $LiNi_{0.5}Co_{0.2}Mn_{0.3}O_2$ Cathode Materials with Micro-Nano Structure for High Performance Li-Ion Batteries. *J. Electroanal. Chem.* **2020**, *878*, 114660.

(16) Du, B.; Mo, Y.; Jin, H.; Li, X.; Qu, Y.; Li, D.; Cao, B.; Jia, X.; Lu, Y.; Chen, Y. Radially Microstructural Design of $LiNi_{0.8}Co_{0.1}Mn_{0.1}O_2$ Cathode Material toward Long-Term Cyclability and High Rate Capability at High Voltage. *ACS Appl. Energy Mater.* **2020**, *3* (7), 6657-6669.

(17) Oh, P.; Myeong, S.; Cho, W.; Lee, M.-J.; Ko, M.; Jeong, H. Y.; Cho, J. Superior Long-Term Energy Retention and Volumetric Energy Density for Li-Rich Cathode Materials. *Nano Lett.* **2014**, *14* (10), 5965-5972.

(18) Hua, W.; Liu, W.; Chen, M.; Indris, S.; Zheng, Z.; Guo, X.; Bruns, M.; Wu, T.-H.; Chen, Y.; Zhong, B.; Chou, S.; Kang, Y.-M.; Ehrenberg, H. Unravelling the Growth Mechanism of Hierarchically Structured $Ni_{1/3}Co_{1/3}Mn_{1/3}(OH)_2$ and Their Application as Precursors for High-Power Cathode Materials. *Electrochim. Acta* **2017**, *232*, 123-131.

(19) Li, J.; Yao, R.; Cao, C. $LiNi_{1/3}Co_{1/3}Mn_{1/3}O_2$ Nanoplates with {010} Active Planes Exposing Prepared in Polyol Medium as a High-Performance Cathode for Li-Ion Battery. *ACS Appl. Mater. Interfaces* **2014**, *6* (7), 5075-5082.

(20) Tian, J.; Su, Y.; Wu, F.; Xu, S.; Chen, F.; Chen, R.; Li, Q.; Li, J.; Sun, F.; Chen, S. High-Rate and Cycling-Stable Nickel-Rich Cathode Materials with Enhanced Li^+ Diffusion Pathway. *ACS Appl. Mater. Interfaces* **2016**, *8* (1), 582-587.

(21) Luo, D.; Li, G.; Fu, C.; Zheng, J.; Fan, J.; Li, Q.; Li, L. $LiMO_2$ (M = Mn, Co, Ni) Hexagonal Sheets with (101) Facets for Ultrafast Charging-Discharging Lithium Ion Batteries. *J. Power Sources* **2015**, *276*, 238-246.

(22) Fu, F.; Xu, G.-L.; Wang, Q.; Deng, Y.-P.; Li, X.; Li, J.-T.; Huang, L.; Sun, S.-G. Synthesis of Single Crystalline Hexagonal Nanobricks of $LiNi_{1/3}Co_{1/3}Mn_{1/3}O_2$ with High

Percentage of Exposed {010} Active Facets as High Rate Performance Cathode Material for Lithium-Ion Battery. *J. Mater. Chem. A* **2013**, *1* (12), 3860.

(23) Soloy, A.; Flahaut, D.; Allouche, J.; Foix, D.; Salvato Vallverdu, G.; Suard, E.; Dumont, E.; Gal, L.; Weill, F.; Croguennec, L. Effect of Particle Size on $LiNi_{0.6}Mn_{0.2}Co_{0.2}O_2$ Layered Oxide Performance in Li-Ion Batteries. *ACS Appl. Energy Mater*. **2022**, *5* (5), 5617-5632

(24) Rodriguez-Carvajal, J. Recent Advances in Magnetic Structure Determination by Neutron Powder Diffraction. *Physica B* **1993**, *192*, 55-69.

(25) Rodriguez-Carvajal, J. https://www.ill.eu/sites/fullprof/php/FullProf_News.htm Version January 2021 Copyleft (c) 2021 JGP-JRC

(26) Scofield, J. H. Hartree-Slater Subshell Photoionization Cross-Sections at 1254 and 1487 eV. *J. Electron. Spectrosc. Relat. Phenom.* **1976**, *8*, 129-137.

(27) Hartmann, L.; Pritzl, D.; Beyer, H.; Gasteiger, H. A. Evidence for Li^+/H^+ Exchange during Ambient Storage of Ni-Rich Cathode Active Materials. *J. Electrochem. Soc.* **2021**, *168*, 070507.

(28) Martinez, A. C.; Grugeon, S.; Cailleu, D.; Courty, M.; Tran-Van, P.; Delobel, B.; Laruelle, S. High Reactivity of the Nickel-Rich $LiNi_{1-x-y}Mn_xCo_yO_2$ Layered Materials Surface towards H_2O/CO_2 Atmosphere and $LiPF_6$-Based Electrolyte. *J. Power Sources* **2020**, *468*, 228204.

(29) Busà, C.; Belekoukia, M.; Loveridge, M. J. The Effects of Ambient Storage Conditions on the Structural and Electrochemical Properties of NMC-811 Cathodes for Li-Ion Batteries. *Electrochim. Acta* **2021**, *366*, 137358.

(30) Rougier, A.; Gravereau, P.; Delmas, C. Optimization of the Composition of the $Li_{1-z}Ni_{1+z}O_2$ Electrode Materials: Structural, Magnetic, and Electrochemical Studies. *J. Electrochem. Soc.* **1996**, *143* (4), 1168-1174.

(31) Wang, T.; Ren, K.; Xiao, W.; Dong, W.; Qiao, H.; Duan, A.; Pan, H.; Yang, Y.; Wang, H. Tuning the Li/Ni Disorder of the NMC811 Cathode by Thermally Driven Competition between Lattice Ordering and Structure Decomposition. *J. Phys. Chem. C* **2020**, *124* (10), 5600-5607.

(32) Peres, J. P.; Delmas, C.; Rougier, A.; Broussely, M.; Perton, F.; Biensan, P.; Willmann, P. The Relationship between the Composition of Lithium Nickel Oxide and the Loss of Reversibility during the First Cycle. *J. Phys. Chem. Solids* **1996**, *57* (6-8), 1057-1060.

(33) Wang, D.; Xin, C.; Zhang, M.; Bai, J.; Zheng, J.; Kou, R.; Peter Ko, J. Y.; Huq, A.; Zhong, G.; Sun, C.-J.; Yang, Y.; Chen, Z.; Xiao, Y.; Amine, K.; Pan, F.; Wang, F. Intrinsic Role of Cationic Substitution in Tuning Li/Ni Mixing in High-Ni Layered Oxides. *Chem. Mater.* **2019**, *31* (8), 2731-2740.

(34) Yin, S.-C.; Rho, Y.-H.; Swainson, I.; Nazar, L. F. X-Ray/Neutron Diffraction and Electrochemical Studies of Lithium De/Re-Intercalation in $Li_{1-x}Co_{1/3}Ni_{1/3}Mn_{1/3}O_2$ (x=0→1). *Chem. Mater.* **2006**, *18* (7), 1901-1910.

(35) Guilmard, M.; Pouillerie, C.; Croguennec, L.; Delmas, C.; Structural and Electrochemical Properties of $LiNi_{0.70}Co_{0.15}Al_{0.15}O_2$. *Solid State Ionics* **2003**, *160*, 39-50.

(36) Guilmard, M.; Croguennec, L.; Delmas, C. Effects of Manganese Substitution for Nickel on the Structural and Electrochemical Properties of $LiNiO_2$. *J. Electrochem. Soc.* **2003**, *150* (10), A1287.

(37) Guilmard, M.; Rougier, A.; Grüne, M.; Croguennec, L.; Delmas, C. Effects of Aluminum on the Structural and Electrochemical Properties of $LiNiO_2$. *J. Power Sources* **2003**, *115*, 305-314.

(38) Croguennec, L.; Suard, E.; Willmann, P.; Delmas, C. Structural and Electrochemical Characterization of the $LiNi_{1-y}Ti_yO_2$ Electrode Materials Obtained by Direct Solid-State Reactions. *Chem. Mater.* **2002**, *14*, 2149-2157.

(39) Dahéron, L.; Dedryvère, R.; Martinez, H.; Ménétrier, M.; Denage, C.; Delmas, C.; Gonbeau, D. Electron Transfer Mechanisms upon Lithium Deintercalation from $LiCoO_2$ to CoO_2 Investigated by XPS. *Chem. Mater.* **2008**, *20* (2), 583-590.

(40) Dedryvère, R.; Foix, D.; Franger, S.; Patoux, S.; Daniel, L.; Gonbeau, D. Electrode/Electrolyte Interface Reactivity in High-Voltage Spinel $LiMn_{1.6}Ni_{0.4}O_4/Li_4Ti_5O_{12}$ Lithium-Ion Battery. *J. Phys. Chem. C* **2010**, *114* (24), 10999-11008.

(41) Quesne-Turin, A.; Flahaut, D.; Croguennec, L.; Vallverdu, G.; Allouche, J.; Charles-Blin, Y.; Chotard, J.-N.; Ménétrier, M.; Baraille, I. Surface Reactivity of Li_2MnO_3 : First-Principles and Experimental Study. *ACS Appl. Mater. Interfaces* **2017**, *9* (50), 44222-44230.

(42) Fang, Z.; Confer, M. P.; Wang, Y.; Wang, Q.; Kunz, M. R.; Dufek, E. J.; Liaw, B.; Klein, T. M.; Dixon, D. A.; Fushimi, R. Formation of Surface Impurities on Lithium-Nickel-Manganese-Cobalt Oxides in the Presence of CO_2 and H_2O. *J. Am. Chem. Soc.* **2021**, *143* (27), 10261-10274.

(43) Jung, R.; Metzger, M.; Maglia, F.; Stinner, C.; Gasteiger, H. A. Oxygen Release and Its Effect on the Cycling Stability of $LiNi_xMn_yCo_zO_2$ (NMC) Cathode Materials for Li-Ion Batteries. *J. Electrochem. Soc.* **2017**, *164* (7), A1361-A1377.

(44) Shin, H.; Park, J.; Sastry, A. M.; Lu, W. Effects of Fluoroethylene Carbonate (FEC) on Anode and Cathode Interfaces at Elevated Temperatures. *J. Electrochem. Soc.* **2015**, *162* (9), A1683-A1692.

(45) Zhang, S. S. A Review on Electrolyte Additives for Lithium-Ion Batteries. *J. Power Sources* **2006**, *162* (2), 1379-1394.

(46) Kim, K.; Park, I.; Ha, S.-Y.; Kim, Y.; Woo, M.-H.; Jeong, M.-H.; Shin, W. C.; Ue, M.; Hong, S. Y.; Choi, N.-S. Understanding the Thermal Instability of Fluoroethylene Carbonate in $LiPF_6$-Based Electrolytes for Lithium Ion Batteries. *Electrochim. Acta* **2017**, *225*, 358-368.

(47) Tasaki, K.; Goldberg, A.; Lian, J.-J.; Walker, M.; Timmons, A.; Harris, S. J. Solubility of Lithium Salts Formed on the Lithium-Ion Battery Negative Electrode Surface in Organic Solvents. *J. Electrochem. Soc.* **2009**, *156* (12), A1019-A1027.

(48) Sinha, N. N.; Burns, J. C.; Dahn, J. R. Storage Studies on Li/Graphite Cells and the Impact of So-Called SEI-Forming Electrolyte Additives. *J. Electrochem. Soc.* **2013**, *160* (4), A709-A714.

(49) Deng, B.; Li, J.; Shang, H.; Liu, W.; Wan, Q.; Chen, M.; Qu, M.; Peng, G. Improving Cyclic Stability of $LiNi_{0.6}Co_{0.2}Mn_{0.2}O_2$-$SiO_x$/Graphite Full Cell Using Tris(Trimethylsilyl)Phosphite and Fluoroethylene Carbonate as Combinative Electrolyte Additive. *Ionics* **2020**, *26*, 2247-2257.

(50) Dedryvère, R.; Gireaud, L.; Grugeon, S.; Laruelle, S.; Tarascon, J.-M.; Gonbeau, D. Characterization of Lithium Alkyl Carbonates by X-Ray Photoelectron Spectroscopy: Experimental and Theoretical Study. *J. Phys. Chem. B* **2005**, *109* (33), 15868-15875.

(51) Gauthier, N.; Courrèges, C.; Demeaux, J.; Tessier, C.; Martinez, H. Influence of the Cathode Potential on Electrode Interactions within a $Li_4Ti_5O_{12}$ vs $LiNi_{3/5}Mn_{1/5}Co_{1/5}O_2$ Li-Ion Battery. *J. Electrochem. Soc.* **2020**, *167* (4), 040504.

(52) Karayaylali, P.; Zhang, Y.; Giordano, L.; Katayama, Y.; Tatara, R.; Yu, Y.; Maglia, F.; Jung, R.; Shao-Horn, Y. The Role of Diphenyl Carbonate Additive on the Interfacial

Reactivity of Positive Electrodes in Li-Ion Batteries. *J. Electrochem. Soc.* **2020**, *167* (4), 040522.

(53) Soloy, A.; Flahaut, D.; Foix, D.; Allouche, J.; Salvato Vallverdu, G.; Dumont, E.; Gal, L.; Weill, F.; Croguennec, L. Reactivity at the Electrode-Electrolyte Interfaces in Li-Ion and gel electrolyte lithium Batteries for $LiNi_{0.6}Mn_{0.2}Co_{0.2}O_2$ with Different Particle Sizes. *ACS Applied Materials & Interfaces* accepted on May the 25th 2022.

(54) Ohzuku, T.; Ueda, A. Solid- State Redox Reactions of $LiCoO_2$ (R3m) for 4 Volt Secondary Lithium Cells. *J. Electrochem. Soc.* **1994**, *141*, 2972.

(55) Reimers, J. N.; Dahn, J. R. Electrochemical and In Situ X- Ray Diffraction Studies of Lithium Intercalation in Li_xCoO_2. *J. Electrochem. Soc.* **1992**, *139* (8), 2091-2097.

(56) Tian, C.; Nordlund, D.; Xin, H. L.; Xu, Y.; Liu, Y.; Sokaras, D.; Lin, F.; Doeff, M. M. Depth-Dependent Redox Behavior of $LiNi_{0.6}Mn_{0.2}Co_{0.2}O_2$. *J. Electrochem. Soc.* **2018**, *165* (3), A696-A704.

(57) Quilty, C. D.; Bock, D. C.; Yan, S.; Takeuchi, K. J.; Takeuchi, E. S.; Marschilok, A. C. Probing Sources of Capacity Fade in $LiNi_{0.6}Mn_{0.2}Co_{0.2}O_2$ (NMC622): An *Operando* XRD Study of Li/NMC622 Batteries during Extended Cycling. *J. Phys. Chem. C* **2020**, *124* (15), 8119-8128.

(58) Croguennec, L.; Pouillerie, C.; Delmas, C. NiO_2 Obtained by Electrochemical Lithium Deintercalation from Lithium Nickelate: Structural Modifications. *J. Electrochem. Soc.* **2000**, *147* (4), 1314-1321.

(59) Croguennec, L.; Pouillerie, C.; Delmas, C. Structural Characterisation of New Metastable NiO_2 Phases. *Solid State Ionics* **2000**, *135*, 259-266.

(60) Xu, M.; Fei, L.; Zhang, W.; Li, T.; Lu, W.; Zhang, N.; Lai, Y.; Zhang, Z.; Fang, J.; Zhang, K.; Li, J.; Huang, H. Tailoring Anisotropic Li-Ion Transport Tunnels on

Orthogonally Arranged Li-Rich Layered Oxide Nanoplates Toward High-Performance Li-Ion Batteries. *Nano Lett.* **2017**, *17* (3), 1670-1677.

(61) Jung, C.; Kim, D.; Eum, D.; Kim, K.; Choi, J.; Lee, J.; Kim, H.; Kang, K.; Hong, S. New Insight into Microstructure Engineering of Ni- Rich Layered Oxide Cathode for High Performance Lithium Ion Batteries. *Adv. Funct. Mater.* **2021**, *31*, 2010095.

TOC

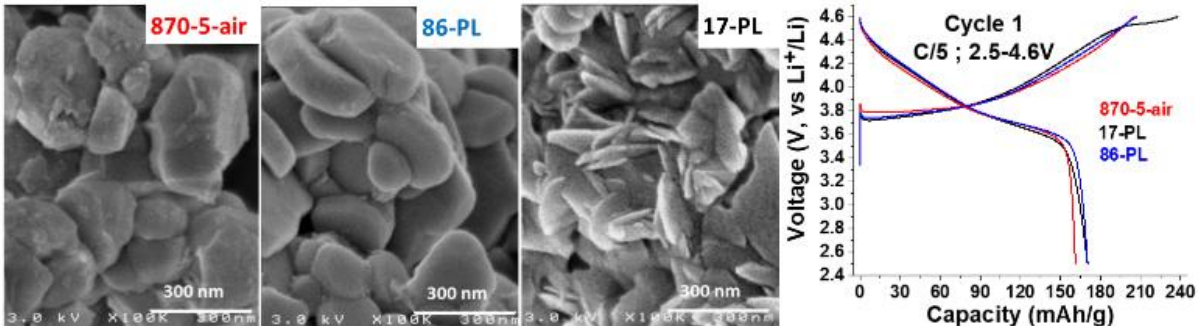

Platelet-shaped $LiNi_{0.6}Mn_{0.2}Co_{0.2}O_2$ particles of 17 and 86 nm thickness were obtained. Their electrochemical performance and reactivity were characterized in Li-ion batteries and compared to those of 280 nm diameter particles showing a more conventional morphology. Particular reactivity was observed for platelet-like morphology at high potential compared to the conventional morphology.